JACS
JOURNAL OF THE AMERICAN CHEMICAL SOCIETY
Article
pubs.acs.org/JACS

Turning on the Protonation-First Pathway for Electrocatalytic CO_2 Reduction by Manganese Bipyridyl Tricarbonyl Complexes

Ken T. Ngo,[†] Meaghan McKinnon,[†] Bani Mahanti,[†] Remya Narayanan,[†] David C. Grills,*[,‡] Mehmed Z. Ertem,*[,‡] and Jonathan Rochford*[,†]

[†]Department of Chemistry, University of Massachusetts Boston, 100 Morrissey Boulevard, Boston, Massachusetts 02125, United States

[‡]Chemistry Division, Energy & Photon Sciences Directorate, Brookhaven National Laboratory, Upton, New York 11973-5000, United States

Supporting Information

ABSTRACT: Electrocatalytic reduction of CO_2 to CO is reported for the complex, {*fac*-Mn^I([$(MeO)_2Ph]_2$bpy)$(CO)_3(CH_3CN)$}(OTf), containing four pendant methoxy groups, where $[(MeO)_2Ph]_2$bpy = 6,6′-bis(2,6-dimethoxyphenyl)-2,2′-bipyridine. In addition to a steric influence similar to that previously established [Sampson, M. D. et al. *J. Am. Chem. Soc.* **2014**, *136*, 5460−5471] for the 6,6′-dimesityl-2,2′-bipyridine ligand in [*fac*-$Mn^I(mes_2bpy)(CO)_3(CH_3CN)$](OTf), which prevents Mn^0−Mn^0 dimerization, the $[(MeO)_2Ph]_2$bpy ligand introduces an additional electronic influence combined with a weak allosteric hydrogen-bonding interaction that significantly lowers the activation barrier for C−OH bond cleavage from the metallocarboxylic acid intermediate. This provides access to the thus far elusive *protonation-first* pathway, minimizing the required overpotential for electrocatalytic CO_2 to CO conversion by Mn(I) polypyridyl catalysts, while concurrently maintaining a respectable turnover frequency. Comprehensive electrochemical and computational studies here confirm the positive influence of the $[(MeO)_2Ph]_2$bpy ligand framework on electrocatalytic CO_2 reduction and its dependence upon the concentration and pK_a of the external Brønsted acid proton source (water, methanol, trifluoroethanol, and phenol) that is required for this class of manganese catalyst. Linear sweep voltammetry studies show that both phenol and trifluoroethanol as proton sources exhibit the largest *protonation-first* catalytic currents in combination with {*fac*-Mn^I([$(MeO)_2Ph]_2$bpy)$(CO)_3(CH_3CN)$}(OTf), saving up to 0.55 V in overpotential with respect to the thermodynamically demanding *reduction-first* pathway, while bulk electrolysis studies confirm a high product selectivity for CO formation. To gain further insight into catalyst activation, time-resolved infrared (TRIR) spectroscopy combined with pulse-radiolysis (PR-TRIR), infrared spectroelectrochemistry, and density functional theory calculations were used to establish the ν(CO) stretching frequencies and energetics of key redox intermediates relevant to catalyst activation.

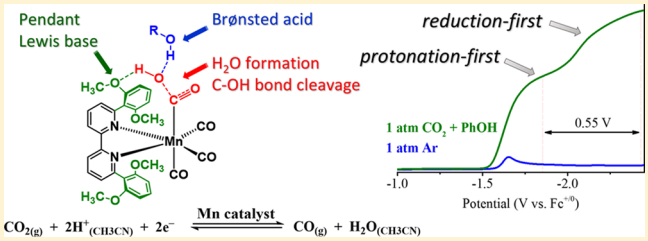

INTRODUCTION

The security of an energy supply, its sustainability, and environmental consequences are concerns both at a national and at a global level in our society today. It is widely accepted that the global environment cannot sustain the current rates of CO_2 uptake into the atmosphere. Having recently surpassed atmospheric CO_2 concentrations of 400 ppm, our environment is progressing further into unknown territory where the consequences of such pollution are yet to be fully realized.[1] Clean and renewable alternative energy sources are therefore needed to mitigate the CO_2 issue and resolve our dependence on fossil fuels.[2] One approach to this problem is the catalytic transformation of CO_2 to carbon monoxide (CO), which is a key raw material alongside hydrogen gas for liquid fuel production by the Fischer−Tropsch reaction.[3] The one-electron reduction of free CO_2 (eq 1) is a thermodynamically demanding reaction, which occurs at an equilibrium potential (E_{eq}) of −1.99 V vs the standard hydrogen electrode (SHE) in water due, in part, to the large reorganization energy involved.[4] Through the application of bioinspired proton-coupled electron transfer (PCET) catalysis, the thermodynamic requirements can be reduced significantly, producing, for example, CO at a more modest potential of −0.52 V vs SHE in water at pH 7 (eq 2, E_{eq} = −0.11 V vs SHE at pH 0).[5] More relevant to this study, the nonaqueous equilibrium potential for CO_2 to CO conversion in acetonitrile has recently been reported,[4] where the technique of isothermal titration calorimetry was used to experimentally determine the apparent pK_a of CO_2 + H_2O in acetonitrile, allowing the previously estimated[6] standard potential in wet acetonitrile to be revised to −1.55 V vs $Fc^{+/0}$ in the presence of 1.0 M H_2O at pH 24 (eq 3).[4] In addition, the equilibrium potential for CO_2 to CO conversion in dry acetonitrile at pH 0 (eq 4) was reported as −0.13 V vs $Fc^{+/0}$ by Matsubara et al.[4] and as −0.12 V vs $Fc^{+/0}$ by Appel and Mayer.[7]

Received: August 25, 2016
Published: January 24, 2017

DOI: 10.1021/jacs.6b08776
J. Am. Chem. Soc. 2017, 139, 2604−2618

$$CO_{2(g)} + e^- \rightleftharpoons CO_2^{\bullet -}{}_{(aq)} \quad E_{eq} = -1.99\ V\ (vs\ SHE) \tag{1}$$

$$CO_{2(g)} + 2H^+{}_{(aq)} + 2e^- \rightleftharpoons CO_{(g)} + H_2O_{(l)} \quad E_{eq} = -0.52\ V\ (vs\ SHE;\ pH = 7) \tag{2}$$

$$3CO_{2(g)} + H_2O_{(CH3CN)} + 2e^- \rightleftharpoons CO_{(g)} + 2HCO_3^-{}_{(CH3CN)} \quad E_{eq} = -1.55\ V\ (vs\ Fc^{+/0};\ pH = 24) \tag{3}$$

$$CO_{2(g)} + 2H^+{}_{(CH3CN)} + 2e^- \rightleftharpoons CO_{(g)} + H_2O_{(CH3CN)} \quad E_{eq} = -0.13\ V\ (vs\ Fc^{+/0};\ pH = 0) \tag{4}$$

Homogeneous transition metal-based catalysts have long been utilized for electrocatalytic CO_2 reduction[8,9] as the metallocarboxylate intermediate reduces the reorganization energy, and thus the required overpotential, by stabilizing a bent configuration of the carboxylate anion.[10] Catalysts have varied in design using electron-rich late transition metal complexes such as cobalt and nickel cyclam or tetra-amine complexes,[11−14] cobalt and iron pincer complexes[15,16] and tetrapyrroles,[17−19] polypyridyl complexes of cobalt,[20−22] rhenium,[23−26] ruthenium,[27−31] osmium,[32] rhodium, and iridium,[33,34] and phosphine complexes of cobalt,[35] nickel,[36] rhodium, and palladium.[37,38] The group VII *fac*-$Re^I(N^N)(CO)_3X$ class of complexes, where N^N = polypyridyl ligand and X = monodentate ligand, have maintained interest for many years due to their high efficiency and selectivity for CO formation. Since the first report of photocatalytic CO_2 reduction with *fac*-$Re^I(bpy)(CO)_3Cl$ (bpy = 2,2′-bipyridine) by Hawecker, Lehn, and Ziessel, there have been many literature reports of related photo-/electrocatalytic systems, with numerous reviews written on the topic.[5,9,23,39−46] A recent development in this field has been the successful application of analogous $[fac\text{-}Mn^I(N^N)(CO)_3X]^n$ complexes (where X = Br^- (n = 0) or X = CH_3CN (n = +1)) as electrocatalysts, taking advantage of the more abundant and economical first row transition metal, manganese. This was first reported by Bourrez et al., who used the *fac*-$Mn^I(N^N)(CO)_3Br$ (N^N = bpy and 4,4′-dimethyl-2,2′-bipyridine (dmbpy)) electrocatalysts to demonstrate that, unlike their Re counterparts, first row $[fac\text{-}Mn^I(N^N)(CO)_3X]^n$ electrocatalysts require the presence of a Brønsted acid in the acetonitrile electrolyte solution to show any catalytic function.[47] This advancement has rightly been attracting significant interest of late inspiring a number of related studies on $[fac\text{-}Mn^I(N^N)(CO)_3X]^n$ systems for electrocatalytic CO_2 reduction.[48−65] In fact, the same group later reported in situ electron paramagnetic resonance evidence of a $[Mn^{II}(dmbpy)(CO)_3(C(O)OH)]^+$ metallocarboxylic acid intermediate derived from the Mn^0−Mn^0 dimer precursor.[54] One notable example inspired by the work of Bourrez et al. is that of Sampson et al., who reported the $[fac\text{-}Mn^I(mes_2bpy)(CO)_3(CH_3CN)](OTf)$ (mes_2bpy = 6,6′-dimesityl-2,2′-bipyridine) complex where the 6,6′-dimesityl substituents on the bpy ligand sterically hinder the formation of a Mn^0−Mn^0 dimer complex from the five-coordinate, one-electron reduced $Mn^0(mes_2bpy)(CO)_3$ species, thus eliminating this side reaction and enhancing catalytic turnover frequency for CO formation.[51] The same group has also introduced a magnesium (Mg^{2+}) Lewis acid cocatalyst with $[fac\text{-}Mn^I(mes_2bpy)(CO)_3(CH_3CN)](OTf)$ to effect a lower overpotential pathway to generate CO and $MgCO_3$ using a sacrificial Mg counter electrode.[63,66,67] Prior work by Fujita et al. had already demonstrated a reduction in overpotential for the $[Ru(bpy)_2(CO)Cl]^+$ electrocatalyst for CO formation in the presence of a Lewis acid.[68] Analogous work by Savéant et al. demonstrated an increase in TOF without a reduction in overpotential for a selection of Lewis acids (Li^+, Na^+, Mg^{2+}, Ca^{2+}, Ba^{2+}) with Fe^0 porphyrin-based CO_2 reduction electrocatalysts.[66,67] Indeed, notable work by Savéant and co-workers has demonstrated record turnover numbers (TONs) and turnover frequencies (TOFs) for electrocatalytic CO_2 to CO conversion by providing pendant Brønsted acid sites at Fe(0) *meso*-tetraarylporphyrin catalysts in a DMF electrolyte.[6,69,70] Inspired by the latter approach, Franco et al. reported on the introduction of a pendant 2,6-dihydroxyphenyl group in a *fac*-$Mn^I(N^N)(CO)_3Br$ electrocatalyst, which, in the absence of an external proton source, yielded 22% Faradaic efficiency for formic acid production upon controlled potential electrolysis in acetonitrile with 70% of the Faradaic current being attributed to CO.[50] A later study by Agarwal et al. using the related asymmetrical 6-(2-hydroxyphenyl)-2,2′-bipyridine ligand demonstrated 86% Faradaic efficiency for CO evolution in a 5% H_2O/acetonitrile-based electrolyte.[62] Interestingly, the latter two studies reported zero and insignificant catalytic activity, respectively, for their methoxy-substituted analogues in which the hydroxyl groups are replaced by methoxy groups. While both studies successfully demonstrated the participation of pendant intramolecular Brønsted acid sites in the proton-coupled reduction of CO_2 to CO, no hypothesis as to the lack of catalytic activity was put forth for their methoxy analogues. We were interested in pursuing this direction further to determine whether multiple pendant, aprotic, electron-rich methoxy ligand substituents might participate electronically and/or allosterically to promote the electrocatalytic conversion of CO_2 to CO with a $[fac\text{-}Mn(N^N)(CO)_3X]^n$ complex. Thus, in this study, four pendant methoxy groups are introduced into the second coordination sphere of a manganese catalyst for the first time in $\{fac\text{-}Mn^I([(MeO)_2Ph]_2bpy)(CO)_3(CH_3CN)\}(OTf)$ (**1-CH_3CN^+**, Chart 1). In addition to establishing the Brønsted acid dependence of catalytic current evolution and product selectivity, most remarkable is how voltammetry conditions can be manipulated for this new catalyst to strongly turn on the hitherto elusive *protonation-first* CO_2 reduction pathway at low overpotential.[71] Bulk electrocatalytic CO_2 reduction is also described for **1-CH_3CN^+** relative to $[fac\text{-}Mn^I(mes_2bpy)(CO)_3(CH_3CN)](OTf)$ (**2-CH_3CN^+**) under

Chart 1. Molecular Structures of Complexes Investigated

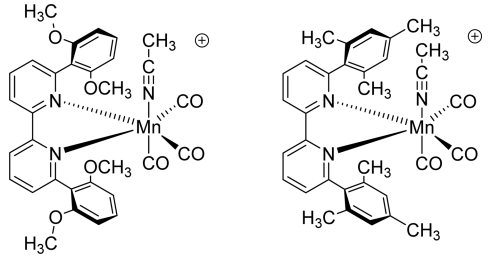

DOI: 10.1021/jacs.6b08776
J. Am. Chem. Soc. 2017, 139, 2604−2618

both low overpotential (*protonation-first*) and high overpotential (*reduction-first*) conditions, with CO:H_2 product distributions reported. Insight into the catalytic pathways was also gained through density functional theory (DFT) calculations. Furthermore, voltammetry studies are presented for a [*fac*-Mn(N^N)$(CO)_3$X]^n complex for the first time in a buffered electrolyte system to quantitatively evaluate the true catalytic overpotential under known nonaqueous pH conditions.

RESULTS AND DISCUSSION

Synthesis. The [$(MeO)_2$Ph]$_2$bpy ligand was prepared by Suzuki coupling of 6,6′-dibromo-2,2′-bipyridine in the presence of excess 2,6-dimethoxyphenyl boronic acid under microwave reflux conditions. The synthesis of **2-CH_3CN^+** was recently reported via bromide/triflate metathesis of the *fac*-$Mn^I(mes_2bpy)(CO)_3Br$ precursor with silver triflate in acetonitrile followed by column chromatography.[51] To avoid chromatography, an alternative synthesis was employed for both *fac*-$Mn^I([(MeO)_2Ph]_2bpy)(CO)_3(OTf)$ (**1-OTf**) and *fac*-$Mn^I(mes_2bpy)(CO)_3(OTf)$ (**2-OTf**) that involved using the $Mn^I(CO)_5(OTf)$ precursor and refluxing with 1 equiv of [$(MeO)_2$Ph]$_2$bpy or mes_2bpy in diethyl ether. $Mn^I(CO)_5(OTf)$ was synthesized according to the literature procedure.[72] It should be kept in mind that both **1-OTf** and **2-OTf** undergo facile solvation in acetonitrile (vide infra) due to the weak binding strength of the triflate anion.[73] Thus, the [*fac*-$Mn^I(R_2bpy)(CO)_3(CH_3CN)]^+$ cations are generated when **1-OTf** and **2-OTf** are dissolved in acetonitrile solution, and are hereafter referred to as **1-CH_3CN^+** and **2-CH_3CN^+**, respectively (Chart 1).

FTIR Spectroscopy. Using FTIR spectroscopy, characteristic ν(CO) ligand vibrational stretching modes are observed for **1-CH_3CN^+** and **2-CH_3CN^+** consistent with their facial tricarbonyl geometries (Figure 1).[74] The solvated complex, **1-CH_3CN^+**, exhibits pseudo-C_s symmetry with a sharp ν(CO) symmetric A′(1) stretching mode at 2038 cm^{-1} and two lower-frequency A′(2) and A″ asymmetric ν(CO) stretching modes at 1954 and 1941 cm^{-1}, respectively. Consistent with the Mn(I) centers of **1-CH_3CN^+** and **2-CH_3CN^+** being isoelectronic, **2-CH_3CN^+** exhibits an almost identical sharp ν(CO) symmetric A(1) stretch at 2039 cm^{-1}. However, the lower-energy asymmetric stretches appear as a single A(2) broad ν(CO) band suggesting pseudo-C_{3v} symmetry for **2-CH_3CN^+**. Computed IR spectra at the M06 level of theory confirm these assignments (see computational methods for details).

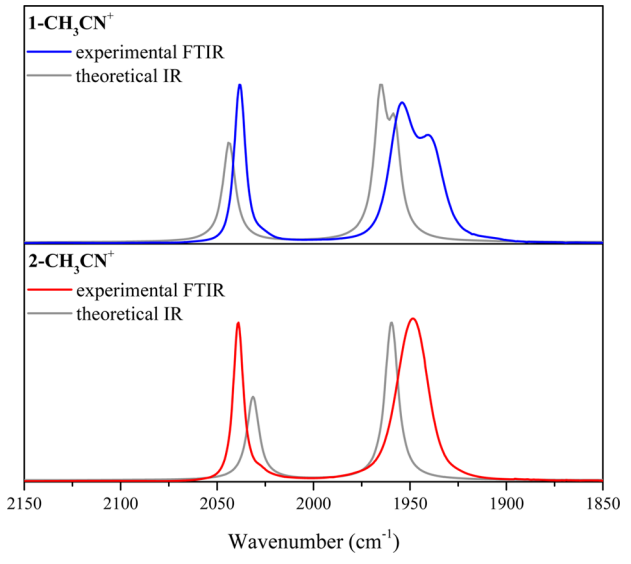

Figure 1. Experimental FTIR spectra of **1-CH_3CN^+** (top) and **2-CH_3CN^+** (bottom) recorded in acetonitrile displaying characteristic ν(CO) stretching modes for their facial (*fac*) tricarbonyl geometries. Computed IR spectra at the M06 level of theory are overlaid for comparison (frequency scaling factor = 0.960).

Cyclic Voltammetry under 1 atm of Argon. Prior to catalysis studies, electrochemical characterization was conducted under an inert argon atmosphere in the absence of an external Brønsted acid to characterize the fundamental redox properties of both **1-CH_3CN^+** and **2-CH_3CN^+**. It was recently established[51] that the bulky mes_2bpy ligand has a strong influence on the redox properties of **2-CH_3CN^+** relative to less-bulky complexes, such as [*fac*-$Mn^I(bpy)(CO)_3(CH_3CN)]^+$, which are prone to Mn^0–Mn^0 dimerization upon one-electron reduction. For example, the Mn^0 radical, *fac*-$Mn^0(dtbpy)(CO)_3$ (where dtbpy = 4,4′-^{t}Bu_2-bpy), exhibits a Mn^0–Mn^0 dimerization rate constant of $2k_{dim} = 1.3 \times 10^9$ M^{-1} s^{-1}.[49] In contrast, a reversible two-electron reduction wave is observed for the reaction, **2-CH_3CN^+** + 2 e^- ⇌ **2**$^-$ + CH_3CN (E = −1.60 V vs $Fc^{+/0}$) where **2**$^-$ is the five-coordinate, 18 valence electron, two-electron reduced [*fac*-$Mn(mes_2bpy)(CO)_3]^-$ anion. This redox reaction follows an electrochemical–chemical–electrochemical (ECE) mechanism whereby, after one-electron reduction, the acetonitrile ligand dissociates followed by rapid one-electron reduction of the neutral Mn(0) intermediate, *fac*-$Mn(mes_2bpy)(CO)_3$, to generate **2**$^-$. A subsequent third irreversible reduction wave is observed at −3.01 V vs $Fc^{+/0}$ (Figure S3). A cyclic voltammogram of **1-CH_3CN^+** recorded in dry acetonitrile with 0.1 M Bu_4NPF_6 as the supporting electrolyte under 1 atm of argon at a glassy carbon disc working electrode and 100 mV s^{-1} scan rate is presented in Figure 2.

The profile of the current–voltage response for **1-CH_3CN^+** shown in Figure 2 is almost identical to that of **2-CH_3CN^+**, suggesting that a similar quasi-reversible two-electron ECE mechanism is occurring to generate the **1**$^-$ anion at E = −1.63 V vs $Fc^{+/0}$. This is consistent with a narrow peak-to-peak

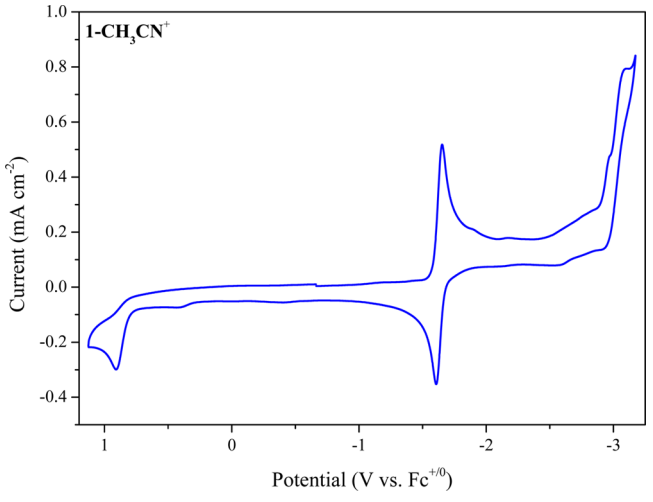

Figure 2. Cyclic voltammogram of **1-CH_3CN^+** recorded in acetonitrile containing 0.1 M Bu_4NPF_6 at a glassy carbon disc working electrode with a scan rate (υ) of 100 mV s^{-1} under 1 atm of argon.

DOI: 10.1021/jacs.6b08776
J. Am. Chem. Soc. 2017, 139, 2604–2618

separation of ΔE = 40 mV (as compared to ΔE = 39 mV for **2-CH_3CN^+**) and is confirmed by both computational analysis and controlled potential FTIR spectroelectrochemistry (vide infra). Scan rate dependence of the current response for the two-electron reduction of **1-CH_3CN^+** to **1^-** confirms quasi-reversible behavior analogous to that of **2-CH_3CN^+** as the anodic−cathodic peak separation increases with scan rate (Figures S4−S6). Similar to **2-CH_3CN^+**, there is no evidence of Mn^0−Mn^0 dimerization, and a linear Randles−Sevcik plot confirms the inertness of **1^-** in acetonitrile under an argon atmosphere. Similarly, a third irreversible one-electron reduction is observed at −3.10 V vs $Fc^{+/0}$. For the record, an irreversible one-electron oxidation of **1-CH_3CN^+** is also observed at +0.91 V vs $Fc^{+/0}$. However, as this oxidation is irrelevant for reductive catalysis, it will not be discussed any further here. Electrochemical data for **1-CH_3CN^+** and **2-CH_3CN^+** recorded under 1 atm argon in a 0.1 M Bu_4NPF_6 acetonitrile electrolyte are summarized in Table 1.

Table 1. Electrochemical Data Recorded by Cyclic Voltammetry for 1-CH_3CN^+ and 2-CH_3CN^+ in Acetonitrile Reported versus the Nonaqueous Ferrocenium/Ferrocene ($Fc^{+/0}$) Pseudo Reference

	E vs $Fc^{+/0}$		
1-CH_3CN^+	+0.91[a]	−1.63[b]	−3.10[c]
2-CH_3CN^+	+0.85[a]	−1.60[b]	−3.01[c]

[a]Irreversible, E_{pa} reported. [b]Quasi-reversible two-electron couple. [c]Irreversible, E_{pc} reported. Conditions: 1 mM sample concentration; 3 mm diameter glassy carbon working electrode; Pt wire counter electrode; Ag/$AgPF_6$ nonaqueous reference electrode; 0.1 V s^{-1} scan rate.

Electrocatalysis. A thorough description of the electroanalytical methods used to extract accurate values of TOF from voltammetry data is beyond the scope of this Article; however, a recent perspective article published by Dempsey and co-workers deals with this topic in depth.[75] The reader is also recommended to consult the relevant literature by Savéant and co-workers dealing specifically with electrocatalytic CO_2 reduction.[70,76−79] Briefly, prior to calculation of the maximum electrocatalytic turnover frequency (TOF_{max}), steady-state experimental conditions must be established with respect to the rates of catalyst activation and consumption. This is typically identified by a characteristic S-shaped catalytic wave or scan-rate independence of the peak catalytic current (i_{cat}). Steady-state conditions were here achieved by increasing the scan rate to achieve pure kinetic conditions such that CO_2 consumption within the diffusion layer at the electrode surface did not hinder access to a peak catalytic current.[80,81] Subsequently, TOF_{max} was determined from the ratio of i_{cat} versus the noncatalytic Faradaic current (i_p) using an established method according to eq 5,[82,83] where F is the Faraday constant, R is the gas constant, T is temperature, υ is the scan rate, n_p is the number of electrons involved in the noncatalytic Faradaic response (2 electrons for both **1-CH_3CN^+** and **2-CH_3CN^+**), and n_{cat} is the number of electrons required to complete a single catalytic cycle (2 electrons as shown in Schemes 1 and 2).

$$TOF_{max} = 0.1992\left(\frac{F\upsilon}{RT}\right)\left(\frac{n_p^3}{n_{cat}^2}\right)\left(\frac{i_{cat}}{i_p}\right)^2 \quad (5)$$

Where steady-state conditions could not be confirmed, foot-of-the-wave-analysis (FOWA) was necessary to estimate TOF_{max} using eq 6:[75,84]

$$\frac{i_{cat}}{i_p} = \frac{2.24\sqrt{\left(\frac{RT}{F\upsilon}\right)TOF_{max}}}{1 + \exp\left[\left(\frac{F}{RT}\right)(E - E^{\circ}_{P/Q})\right]}\left(\frac{n_{cat}}{n_p^{3/2}}\right) \quad (6)$$

where $E^{\circ}_{P/Q}$ represents the standard reduction potential of the active catalyst recorded under noncatalytic conditions (Table 1). Also, in the interest of comparison to other literature catalysts, the simple ratio of i_{cat}/i_p is highlighted; importantly, it should be kept in mind that the latter is scan rate dependent and is reported throughout this Article only at a scan rate of υ = 0.5 V s^{-1} for consistency unless stated otherwise. A complete collection of linear sweep voltammetry data for both **1-CH_3CN^+** and **2-CH_3CN^+** is provided in Figures S9−S14. A first-order rate dependence of the catalytic current was also independently confirmed as a function of Mn complex concentration and CO_2 concentration for both **1-CH_3CN^+** and **2-CH_3CN^+** (Figures S7 and S8). It should also be pointed out that CO was not observed during bulk electrolysis control experiments in the absence of a manganese catalyst.

Electrocatalysis with H_2O as a Proton Source. For many years, it was believed that manganese polypyridyl tricarbonyl complexes were inactive for catalytic CO_2 reduction, unlike their isoelectronic rhenium counterparts. However, Bourrez et al. established that the proton concentration is rate limiting for manganese polypyridyl-mediated CO_2 reduction electrocatalysis, and that in the presence of a Brønsted acid, efficient catalytic reduction of CO_2 to CO occurs.[47] Riplinger et al. have since established that, in contrast to their rhenium analogues, protonation is required for the binding of CO_2 to the two-electron reduced active manganese catalyst.[52,71] Thus, before entering the catalytic cycle, two-electron reduction is required to generate the five-coordinate anionic active catalyst, for example, [*fac*-$Mn(mes_2bpy)(CO)_3]^-$ (**2^-**), in situ (Scheme 1, intermediate i). The **2^-** anion then reacts with CO_2 in the presence of a proton source to generate the neutral six-coordinate *fac*-$Mn^I(mes_2bpy)(CO)_3(CO_2H)$ metallocarboxylic acid intermediate (Scheme 1, intermediate ii). To facilitate rapid hydroxide abstraction from the metallocarboxylic acid intermediate and subsequently generate the desired *fac*-$Mn(mes_2bpy)(CO)_4$ tetracarbonyl intermediate (Scheme 1, intermediate iv), one-electron reduction to the [*fac*-$Mn(mes_2bpy)(CO)_3(CO_2H)]^-$ metallocarboxylic acid anion (Scheme 1, intermediate iii) occurs. It is this latter step that provides the reduction-first label to this catalytic pathway. Subsequent protonation, resulting in C−OH bond cleavage and H_2O ejection, is rate limiting (Scheme 1, intermediates iii,iv) and requires a minimum concentration (pK_a dependent) of weak Brønsted acid in solution to proceed. Thus, the catalytic cycle, proposed by Kubiak[51] and further corroborated computationally by Riplinger and Carter,[60] demonstrates a mandatory two-electron reduction of the Mn(I) polypyridyl complex merely to enter the catalytic cycle and that an implicit overpotential is required to overcome the reduction-first and rate-determining protonation-second steps to generate the tetracarbonyl intermediate (Scheme 1, intermediate iv) prior to reductive CO loss and catalyst regeneration (Scheme 1, intermediates iv−i).[51,52,71]

With this knowledge in hand, the electrocatalytic properties of both catalytic precursors, **1-CH_3CN^+** and **2-CH_3CN^+**, were

DOI: 10.1021/jacs.6b08776
J. Am. Chem. Soc. 2017, 139, 2604−2618

Scheme 1. Catalyst Activation and the Reduction-First Catalytic Cycle for Electrocatalytic Reduction of CO_2 to CO by Manganese Polypyridyl Catalysts[a]

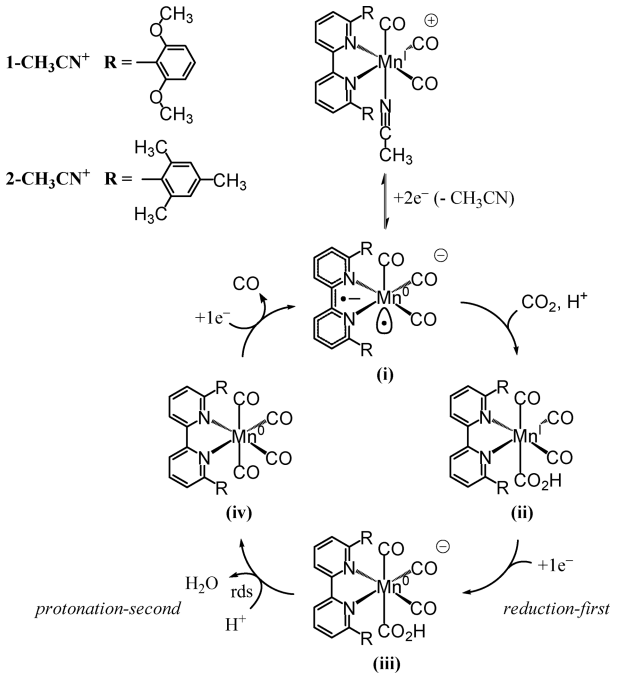

[a]rds = rate-determining step.

probed by linear sweep voltammetry in acetonitrile using H_2O as the sacrificial Brønsted acid. To demonstrate the reduction-first pathway described in Scheme 1, linear sweep voltammetry of **1-CH_3CN^+** under 1 atm of CO_2 in the presence of 6.33 M H_2O (optimized for maximum catalytic current) is presented in Figure 3 at a variety of scan rates. In all cases, a significant growth of catalytic current is observed in the region of −2.3 V, cathodic of the two-electron reduction wave to produce $\mathbf{1}^-$ by −0.7 V (Figure 3, top), with a corresponding TOF_{max} of 258 ± 11 s^{-1} (i_{cat}/i_p = 5.9). This observation is consistent with the reduction-first pathway requiring an additional overpotential to drive the rate-determining protonation/H_2O abstraction steps described above in Scheme 1 (intermediates ii,iii,iv). Upon repeating this experiment with **2-CH_3CN^+**, a similar catalytic current is observed, peaking at 5.95 M H_2O concentration with a decreased TOF_{max}, relative to **1-CH_3CN^+**, of 93 ± 1 s^{-1} (i_{cat}/i_p = 3.5) (Figure 3, bottom). For both **1-CH_3CN^+** and **2-CH_3CN^+**, the scan rate independence of TOF_{max} was only observed in the range of υ = 0.5−1.0 V s^{-1} as illustrated in plots of TOF versus scan rate (Figure 3).

The pendant methoxy groups of **1-CH_3CN^+** clearly have a positive influence on the TOF_{max}, giving rise to a 2.8-fold increase relative to **2-CH_3CN^+** under optimized H_2O concentration conditions. It is worth noting that a common practice in the literature for electrocatalytic CO_2 to CO conversion has been to solely employ 5% v/v H_2O in 0.1 M Bu_4NPF_6 acetonitrile electrolyte. As a point of reference, this corresponds to a concentration of only 2.77 M H_2O. On the basis of the weak catalytic current observed for the tetramethoxy catalyst $\mathbf{1}^-$ at this concentration of H_2O, it is unsurprising, in hindsight, that negligible catalytic activity was observed for a previously reported analogous monomethoxy-substituted catalyst under such conditions.[62] Whether the influence of the pendant methoxy groups is purely electronic or involves a second coordination sphere hydrogen-bonding effect is difficult to confirm. Computational studies do show evidence of noncovalent hydrogen bonding (discussed further below) between the C−OH of the metallocarboxylic acid and the pendant methoxy groups during C−OH bond cleavage. However, an inductive electronic influence of the pendant methoxy groups cannot be ruled out.

Electrocatalysis with a Nonaqueous Proton Source. Of significant note in the voltammogram of **1-CH_3CN^+** under 1 atm of CO_2 in the presence of 6.33 M H_2O (Figure 3) is the observation of a weak catalytic current growing in at −1.6 V upon generation of $\mathbf{1}^-$. In contrast, this behavior is not observed upon in situ generation of $\mathbf{2}^-$. This prompted us to explore electrocatalysis with stronger Brønsted acids. In addition to water ($pK_{a(DMSO)}$ = 31.4;[85] $pK_{a(CH3CN)}$ not reported, n.r.), methanol (MeOH, $pK_{a(DMSO)}$ = 29.0;[85] $pK_{a(CH3CN)}$ n.r.), trifluoroethanol (TFE, $pK_{a(DMSO)}$ = 23.5;[86] $pK_{a(CH3CN)}$ = 35.4 est.[61]), and phenol (PhOH, $pK_{a(DMSO)}$ = 18.0;[87] $pK_{a(CH3CN)}$ = 29.1[88]) were also chosen to study the Brønsted acid concentration dependence of the electrocatalytic TOF for both **1-CH_3CN^+** and **2-CH_3CN^+**. pK_a data in acetonitrile are not available for each Brønsted acid employed. However, pK_a data reported in DMSO are often assumed to be representative of the trend in acetonitrile. The actual Brønsted acid pK_a values will be influenced by dissolved CO_2 (~0.28 M at 1 atm), especially when using water,[4] so the reported nonaqueous pK_a values should be used with caution. From a qualitative perspective, however, there is ample evidence from this study and previous reports that the trend of nonaqueous pK_a's in acetonitrile follows as H_2O > MeOH > TFE > PhOH.[51,89] This is clearly evident in Figure 4 where linear sweep voltammograms are presented for **1-CH_3CN^+** at optimized concentrations of the four Brønsted acids, determined by careful addition of H_2O and the nonaqueous Brønsted acids at incrementing concentrations (Figure S15) to optimize the observed catalytic current. Analogous data for **2-CH_3CN^+** are presented in Figure S16.

The reduction-first TOF_{max} for **2-CH_3CN^+** is already established[51] to increase with decreasing pK_a of the Brønsted acid employed for H_2O, MeOH, and TFE, as observed here. A reduction-first TOF_{max} of 910 ± 4 s^{-1} (i_{cat}/i_p = 10.8) is here reported for **2-CH_3CN^+** in the presence of 2.03 M PhOH as a proton source. This decreased significantly in the presence of TFE (2 M) and MeOH (2.09 M) to 453 ± 5 s^{-1} (i_{cat}/i_p = 7.7) and 115 ± 2 s^{-1} (i_{cat}/i_p = 3.8), respectively. Electrocatalysis for **2-CH_3CN^+** has previously been reported[51] with significantly higher TOFs for the reduction-first pathway; however, we were unsuccessful at reproducing these results (Figure S17, Table S1). A similar trend was observed for the reduction-first pathway of **1-CH_3CN^+** with TOFs of 1257 ± 26 s^{-1} (i_{cat}/i_p = 12.6) in the presence of 1.37 M PhOH, 694 ± 7 s^{-1} (i_{cat}/i_p = 9.4) in the presence of 1.35 M TFE, and 259 s^{-1} (i_{cat}/i_p = 5.7) with 2.09 M MeOH. Consistent with the H_2O data presented in Figure 3 above, **1-CH_3CN^+** outperforms **2-CH_3CN^+** when using either PhOH, TFE, or MeOH. Moreover, **1-CH_3CN^+** is capable of reaching its optimum catalytic turnover at a reduced PhOH concentration of 1.37 M relative to that for **2-CH_3CN^+** at 2.03 M. This overall trend is effectively illustrated in scatter plots of "i_{cat}/i_p versus Brønsted acid concentration" for both **1-CH_3CN^+** and **2-CH_3CN^+** (Figure S15).

Outstanding among these Brønsted acid pK_a and concentration dependence studies is the evolution of a strong catalytic wave for **1-CH_3CN^+**, growing in at reduced overpotential

DOI: 10.1021/jacs.6b08776
J. Am. Chem. Soc. 2017, 139, 2604−2618

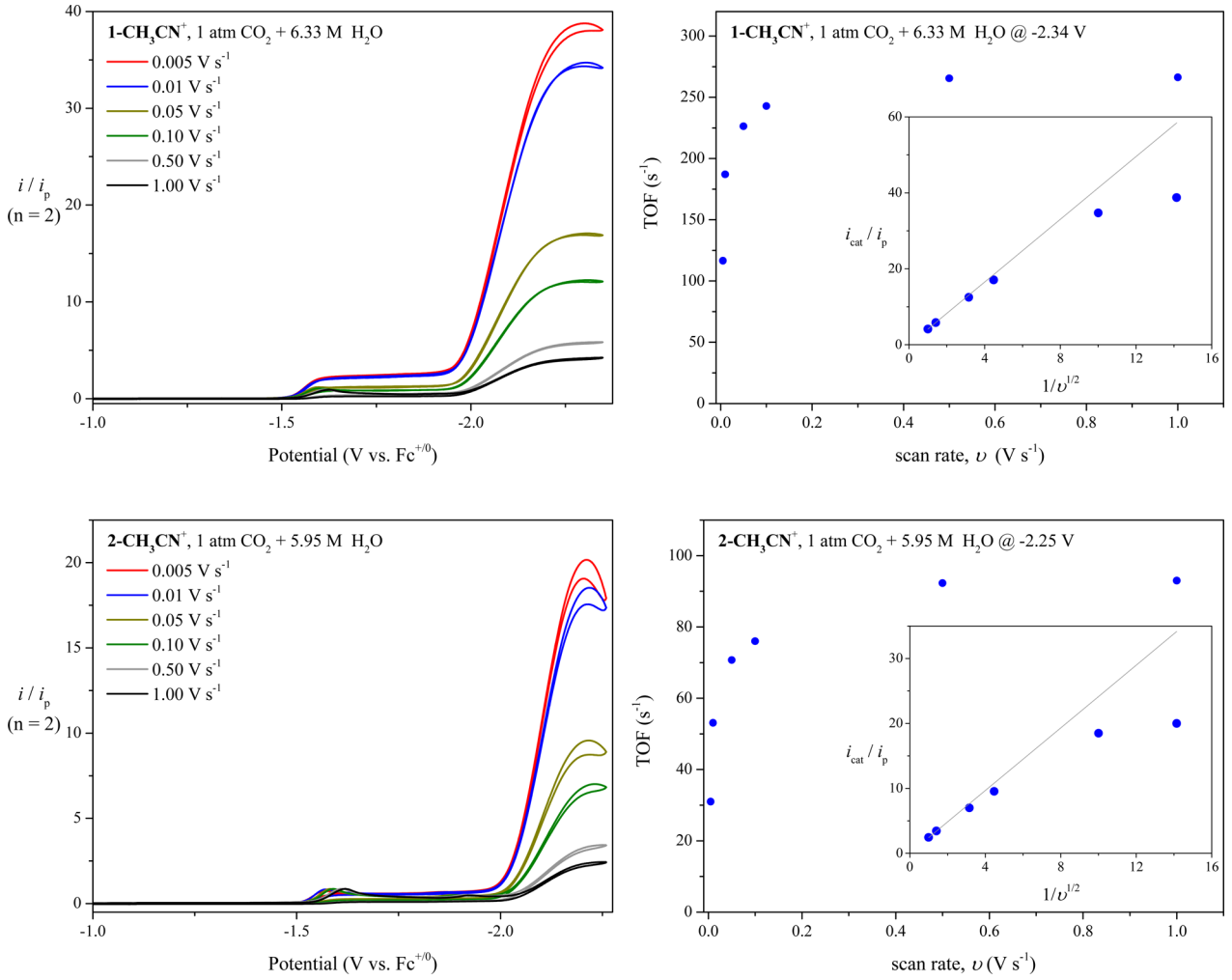

Figure 3. Linear sweep voltammetry of **1-CH_3CN^+** (top) and **2-CH_3CN^+** (bottom) recorded in acetonitrile containing 0.1 M Bu_4NPF_6 and the specified concentrations of H_2O, under 1 atm of CO_2 at a glassy carbon disc working electrode over a scan rate (υ) range 0.1−1.0 V s^{-1}. In both cases, the H_2O concentration was optimized for maximum catalytic current. The *y*-axis current (i) is normalized with respect to the noncatalytic Faradaic current (i_p) to allow a direct comparison of i_{cat}/i_p ratios for each combination of catalyst and proton source where n = 2 is the electron stoichiometry of the i_p Faradaic ECE event under 1 atm of argon. Alongside are plots of TOF versus scan rate, with an inset of i_{cat}/i_p versus inverse square root of the scan rate, to demonstrate steady-state conditions at faster (0.5 and 1.0 V s^{-1}) scan rates.

directly from the two-electron reduced active catalyst $\mathbf{1}^-$, as illustrated in Figure 4, especially in the presence of TFE and PhOH as proton sources. This catalytic wave is here assigned to the hitherto elusive protonation-first mechanistic pathway as theoretically predicted by Riplinger and Carter.[71] While the protonation-first catalytic cycle may result in a lower TOF_{max}, due to a decreased electrochemical driving force for CO_2 activation, it is much desired over the reduction-first pathway due to the opportunity for a significant saving in overpotential, which may benefit in terms of increased catalyst stability, higher turnover numbers, and opening the possibility to drive this cycle efficiently by photochemical means. As with the reduction-first pathway, the active catalyst is again the two-electron reduced, five-coordinate anion, for example, $\mathbf{1}^-$ [*fac*-$Mn([(MeO)_2Ph]_2bpy)(CO)_3]^-$ (Scheme 2, intermediate i). Similarly, the $\mathbf{1}^-$ anion is then predicted to react with CO_2 and a proton source to generate the neutral six-coordinate *fac*-$Mn^I([(MeO)_2Ph]_2bpy)(CO)_3(CO_2H)$ metallocarboxylic acid intermediate **1-CO_2H** (Scheme 2, intermediate ii). At this juncture, the protonation-first pathway takes over where the rate-determining step of C−OH bond cleavage and H_2O ejection is facilitated by the pendant methoxy groups of **1-CO_2H**, through weak hydrogen bonding, generating the six-coordinate tetracarbonyl cation intermediate, {*fac*-$Mn^I([(MeO)_2Ph]_2bpy)(CO)_4\}^+$ (Scheme 2, intermediate iii). By generating the positively charged intermediate, **1-CO^+** (Scheme 2, intermediate iii), the protonation-first pathway enables a facile reduction-second step, significantly anodic of the reduction-first pathway, to generate the six-coordinate neutral tetracarbonyl intermediate, *fac*-$Mn([(MeO)_2Ph]_2bpy)(CO)_4$ (**1-CO**, Scheme 2, intermediate iv), which eliminates the CO product upon another one-electron reduction event, regenerating the active catalyst, $\mathbf{1}^-$ (Scheme 2, intermediates iv−i).

As shown in Figure 4, linear sweep voltammetry of **1-CH_3CN^+** under 1 atm of CO_2 in the presence of 1.37 M optimized PhOH concentration shows an excellent growth of protonation-first catalytic current maximizing at around −1.85 V (estimated by multiple-peak deconvolution; the true maximum is difficult to ascertain due to overlap with the reduction-first catalytic response). This overlap of catalytic peaks renders the application of eq 5 impossible to ascertain

DOI: 10.1021/jacs.6b08776
J. Am. Chem. Soc. 2017, 139, 2604−2618

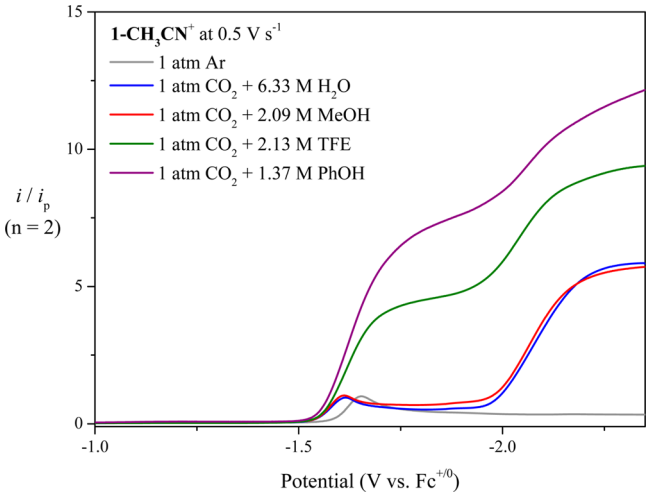

Figure 4. Linear sweep voltammetry of **1-CH_3CN^+** recorded in acetonitrile containing 0.1 M Bu_4NPF_6 with optimized Brønsted acid concentrations at a glassy carbon disc working electrode with a scan rate (υ) of 0.5 V s^{-1} under 1 atm of CO_2. Voltammetry under 1 atm of argon in the absence of Brønsted acid is also included for reference.

Scheme 2. Catalyst Activation and the Protonation-First Catalytic Cycle for Electrocatalytic Reduction of CO_2 to CO by Manganese Polypyridyl Catalysts[a]

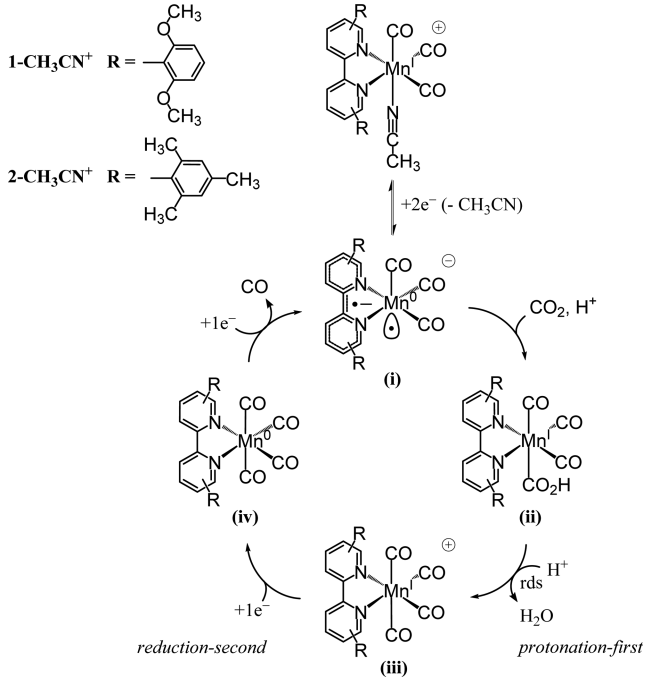

[a]rds = rate-determining step.

TOF_{max} as the peak catalytic current (i_{cat}) is not obtainable. Thus, in the case of the protonation-first pathway, we have employed foot-of-the-wave analysis (FOWA) to estimate accurate TOF_{max} values using eq 6 under appropriate experimental conditions. An example of FOWA is presented for **1-CH_3CN^+** in the presence of 1.37 M PhOH where, due to the underlying onset current from the overlapping reduction-first catalytic wave, the experimental fit exhibits a positive hysteresis with respect to the theoretical linear FOWA fit (Figure 5).

Using FOWA, a TOF_{max} of 138 ± 4 s^{-1} is estimated for the protonation-first pathway for **1-CH_3CN^+** in the presence of 1.37 M PhOH. Although this represents an order of magnitude drop in TOF_{max} relative to the reduction-first catalytic pathway under identical conditions, it does come with the benefit of saving 0.55 V in overpotential. Consistent with its weaker acidity, a TOF_{max} of 82 ± 2 is estimated for **1-CH_3CN^+** in the presence of 2.13 M TFE (Figure S18). As very weak catalytic currents were observed for the protonation-first pathways of **1-CH_3CN^+** combined with MeOH or H_2O, or **2-CH_3CN^+** combined with PhOH or TFE, accurate values of TOF_{max} could not be determined in these cases by FOWA. Suffice to say, catalysis was very slow (<5 s^{-1}); however, bulk electrolysis studies with **2-CH_3CN^+** and PhOH or TFE still gave rise to observable quantities of CO and H_2 (vide infra).

An overlaid scatter plot of the "protonation-first pathway i_{cat}/i_p versus Brønsted acid concentration" is presented in Figure 6 following the growth of the protonation-first catalytic wave for both **1-CH_3CN^+** and **2-CH_3CN^+** with respect to PhOH and TFE concentrations. Importantly, this plot clearly distinguishes the superior kinetic performance of **1-CH_3CN^+** relative to **2-CH_3CN^+** for the protonation-first pathway when using either PhOH or TFE as a proton source. Brønsted acids MeOH and H_2O are less effective at promoting the protonation-first pathway for **1-CH_3CN^+**, whereas **2-CH_3CN^+** shows no catalytic activity at low overpotential under these conditions, most likely due to the higher pK_a values of these acids (Figures 3, S9–S14). A complete summary of all electrocatalysis potential and kinetic data derived from linear sweep voltammetry experiments of **1-CH_3CN^+** and **2-CH_3CN^+** with various Brønsted acids is provided in Table 2.

A mutual electronic/H-bonding influence of the pendant methoxy groups in **1-CH_3CN^+** is here proposed to lower the activation barrier for C–OH bond cleavage from the metallocarboxylic acid intermediate when stronger proton sources, for example, trifluoroethanol and phenol, are used, thus promoting a lower overpotential protonation-first catalytic pathway for CO_2 to CO conversion. This proposed mechanism is discussed in more detail in the Theoretical Investigation section.

Bulk Electrolysis. With a fast-growing interest in molecular catalysts for electrocatalytic CO_2 conversion, it is critical to appreciate that the simple observation of catalytic current in a voltammogram alone is not sufficient to demonstrate CO_2 reactivity.[90] Thus, quantitative in situ gas chromatography analysis has been completed for both **1-CH_3CN^+** and **2-CH_3CN^+** in the presence of optimized Brønsted acid concentrations under 1 atm of CO_2 during controlled potential electrolysis at various applied potentials (derived from voltammetry studies). For example, it is demonstrated that some of the TOFs here reported actually incorporate current density from competitive proton reduction via the hydrogen evolution reaction. It should also be highlighted that formic acid could not be detected in any case by ^1H NMR studies. A summary of Faradaic yields for CO and H_2 evolution under a variety of bulk electrolysis conditions is provided in Table 3 for both **1-CH_3CN^+** and **2-CH_3CN^+**.

It should be clarified that the data in Table 3 are single point analyses reported after 1 h of electrolysis for each experiment. A more detailed summary of the real-time CO:H_2 product evolution is provided in Figures S19–S30 including product turnover numbers (TONs). In general, TONs are very low across the board for both **1-CH_3CN^+** and **2-CH_3CN^+**, leaving

DOI: 10.1021/jacs.6b08776
J. Am. Chem. Soc. 2017, 139, 2604–2618

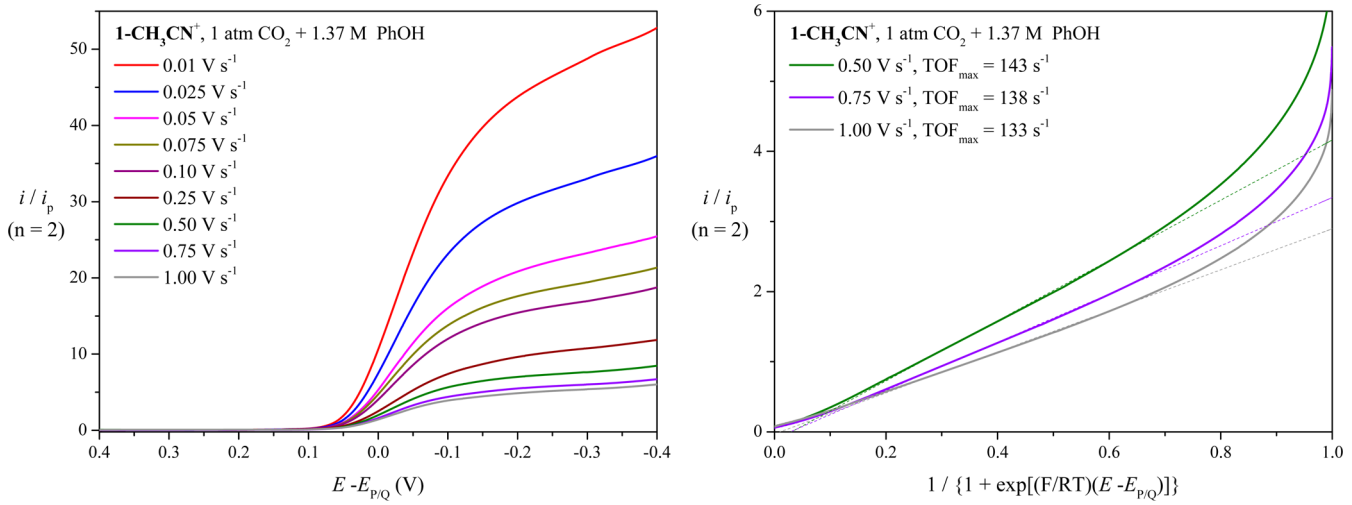

Figure 5. (left) Linear sweep voltammograms of the protonation-first catalytic wave for **1-CH_3CN^+** in the presence of 1.37 M PhOH recorded at various scan rates plotted against $E - E_{P/Q}$. (right) Foot-of-the-wave analysis under equivalent experimental conditions with a linear fit (dashed line) extrapolated from an $E - E_{P/Q}$ range from 0.035 to −0.020 V. For clarity, and comparison with reduction-first data, FOWA is only presented at scan rates in the range of 0.5 − 1.0 V s^{-1}.

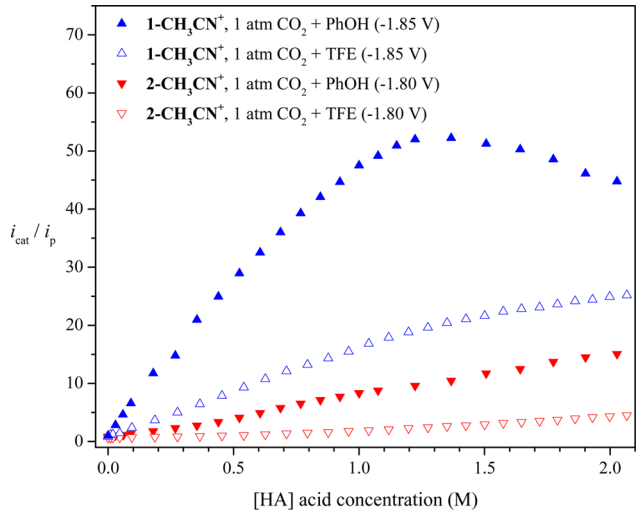

Figure 6. Plots of "protonation-first pathway i_{cat}/i_p versus Brønsted acid concentration" determined by linear sweep voltammetry of **1-CH_3CN^+** and **2-CH_3CN^+** in acetonitrile containing 0.1 M Bu_4NPF_6 and varying concentrations of PhOH and TFE, at a glassy carbon disc working electrode recorded at a scan rate (υ) of 0.01 V s^{-1} under 1 atm of CO_2. All data were monitored at the indicated potentials.

little merit to their discussion. Unfortunately, this is a common problem across the literature with [*fac*-Mn^I(N^N)$(CO)_3X]^n$ electrocatalysts for CO_2 conversion due to their propensity to undergo hydrolytic decomposition. In fact, the maximum reported TON for a manganese-based polypyridyl CO_2 reduction electrocatalyst is 471 over 4 h for Nafion-supported *fac*-Mn^I(bpy)$(CO)_3$Br at a glassy carbon electrode in a pH 7 phosphate buffer electrolyte.[91] The highest reported TON for a homogeneous [*fac*-Mn^I(N^N)$(CO)_3X]^n$ electrocatalyst is just 30 for **2-CH_3CN^+** in acetonitrile in the presence of Mg^{2+} as a Lewis acid cocatalyst.[63] The true merit of investigating [*fac*-Mn^I(N^N)$(CO)_3X]^+$ catalysts for CO_2 conversion at this stage of their development is their very low overpotential, high TOFs, and high product selectivity. Taking Faradaic yields for CO production alone into account, **1-CH_3CN^+** performs very well via the protonation-first pathway, exhibiting an 88% Faradaic yield for CO in the presence of either 1.37 M PhOH or 2.13 M TFE. Competing H_2 evolution, albeit weak, is observed in both of the latter cases with 5% and 13% Faradaic yields with PhOH and TFE, respectively. The CO product selectivity of **1-CH_3CN^+** is reduced slightly to 85% upon application of a greater overpotential via the reduction-first pathway in the presence of 1.37 M PhOH. However, when using 2.13 M TFE or 2.09 M MeOH as a proton source, **1-CH_3CN^+** exhibits superior product selectivity with 100% and 99% selectivity for CO evolution. For both **1-CH_3CN^+** and **2-CH_3CN^+**, the large concentration of H_2O required to optimize the catalyst TOF results in a significant drop in catalyst selectivity with significant H_2 evolution observed in both cases, 38% and 27% Faradaic yields, respectively. In comparison to **2-CH_3CN^+**, catalyst **1-CH_3CN^+** performs equally well at the reduction-first pathway in the presence of optimized concentrations of PhOH, TFE, and MeOH with Faradaic yields in the range of 80−91% for CO evolution. Thus, while there is certainly motivation to use a stronger Brønsted acid to overcome the rate-determining step of either catalytic pathway (Scheme 1, intermediates ii,iii,iv or Scheme 2, intermediates i,ii,iii), this study emphasizes that extreme care must be exercised to identify optimum conditions for selective CO evolution (if that is the desired product), precluding any competitive side reactions, for example, hydrogen evolution or formate production (not observed here). For example, TFE and MeOH as proton sources demonstrate superior selectivity for CO formation in combination with **1-CH_3CN^+** via the reduction-first catalytic pathway, albeit with a slightly lower TOF than when using an optimum concentration of PhOH.

Electrocatalysis with a Buffered Electrolyte. Conducting electrocatalysis in the presence of excess weak Brønsted acid prevents determination of the electrolyte pH, thus precluding knowledge of the standard CO_2 reduction potential under the same conditions. The use of a buffered electrolyte system with an established pH is recommended[92] for determining the true overpotential (η) of a catalytic system. This requires knowledge of the CO_2 to CO equilibrium potential ($E_{CO_2/CO}$) under identical pH conditions. Using the method of Appel and Helm,[92] a convenient way to compare the

DOI: 10.1021/jacs.6b08776
J. Am. Chem. Soc. 2017, 139, 2604−2618

Table 2. Summary of Electrocatalysis Data Derived from Linear Sweep Voltammogram Experiments for Both the Protonation-First and the Reduction-First Pathways[a]

	1-CH_3CN^+				2-CH_3CN^+			
	PhOH	TFE	MeOH	H_2O	PhOH	TFE[c]	MeOH[c]	H_2O[c]
protonation-first (E_{max}, V)	−1.85	−1.85	−1.70	−1.85	−1.75	−1.65		
$E_{cat/2}$ (V)	−1.64	−1.63	−1.57	−1.63	−1.60	−1.58		
[HA] (M)[d]	1.37	2.13	2.09	6.33	2.03	2.00		
TOF max (s^{-1})[e]	138 ± 4	82 ± 2	<5	<1	<3	<1		
reduction-first (E_{max}, V)	−2.40	−2.36	−2.36	−2.34	−2.77	−2.32	−2.26	−2.25
$E_{cat/2}$ (V)	n.o.[b]	n.o.[b]	−2.07	−2.08	−2.29	−2.11	−2.10	−2.11
[HA] (M)[d]	1.37	2.13	2.09	6.33	2.03	2.00	2.09	5.95
i_{cat}/i_p (0.5 V s^{-1})	12.6	9.4	5.7	5.9	10.8	7.7	3.8	3.5
TOF max (s^{-1})[f]	1257 ± 26	694 ± 7	259 ± 4	258 ± 11	910 ± 4	453 ± 5	115 ± 2	93 ± 1

[a]All potentials are reported versus the ferrocenium/ferrocene pseudo reference recorded at 0.5 V s^{-1}. [b]$E_{cat/2}$ is not observable (n.o.) due to overlap of both protonation- and reduction-first catalytic waves. [c]Catalytic current is negligible for the protonation-first pathway of **2-CH_3CN^+** with MeOH or H_2O as a proton source. [d][HA] refers to the bulk concentration of weak Brønsted acid in the electrolyte and should not be confused with [H^+]. [e]Reported as an average with standard deviation from foot-of-the-wave-analysis, hence i_{cat}/i_p not reported. [f]Reported as an average with standard deviation recorded at steady-state conditions from scan rate-dependent studies, typically 0.5 − 1.0 V s^{-1} for **1-CH_3CN^+** and 0.25−1.0 V s^{-1} for **2-CH_3CN^+**.

Table 3. Summary of Controlled Potential Electrolysis Data[a]

	1-CH_3CN^+			2-CH_3CN^+		
	[HA][b] (M)	potential (V vs $Fc^{+/0}$)	Faradaic yield CO:H_2 (%)	[HA][b] (M)	potential (V vs $Fc^{+/0}$)	Faradaic yield CO:H_2 (%)
PhOH	1.37	−1.64[c]	88:5	2.03	−1.75	74:21
		−2.40	85:6		−2.77	91:0
TFE	2.13	−1.63[c]	88:13	2.00	−1.65	97:2
		−2.36	100:0		−2.32	80:8
MeOH	2.09	−2.36	99:0	2.09	−2.26	80:6
H_2O	6.33	−2.34	61:38	5.95	−2.25	73:27

[a]Experimental conditions: 5 mL of 1 mM catalyst in 0.1 M Bu_4NPF_6 acetonitrile supporting electrolyte with stated Brønsted acid concentration [HA] under 1 atm of CO_2. [b][HA] refers to the bulk concentration of Brønsted acid in the electrolyte and should not be confused with [H^+]. [c]Controlled potential electrolysis was conducted at $E_{cat/2}$ to ensure only protonation-first catalysis.

overpotentials (η) required for efficient catalysis with various homogeneous catalysts is to define η as the difference between the equilibrium potential $E_{CO_2/CO}$ (the standard potential $E^{\circ}_{CO_2/CO}$ applies at pH = 0) and the catalytic peak half-wave potential ($E_{cat/2}$) as shown in eq 7.[4,92]

$$\eta = |E_{CO_2/CO} - E_{cat/2}| \quad (7)$$

It is imperative to appreciate here that the equilibrium potential $E_{CO_2/CO}$ is pH-dependent (eqs 2 and 4). As such, the standard reduction potential of $E^{\circ}_{CO_2/CO}$ = −0.13 V vs $Fc^{+/0}$ reported by Matsubara et al.[4] (or the almost identical value of −0.12 V vs $Fc^{+/0}$ reported by Appel and Mayer[7]) for the reduction of CO_2 to CO in dry acetonitrile (eq 4) represents a very specific reaction condition. Fortunately, by using a buffered Brønsted acid with an established pK_a in acetonitrile, it is possible to correct $E^{\circ}_{CO_2/CO}$ using the pH-dependent Nernst equation for the two-electron/two-proton reduction of CO_2 (eq 8), thereby allowing calculation of η where the pH is buffer-stabilized:

$$E_{CO_2/CO} = E^{\circ}_{CO_2/CO} - \left(\frac{2.303RT}{2F}\right)\cdot 2\text{pH} \quad (8)$$

The buffer system, benzoic acid:tetrabutylammonium benzoate, [BzOH]:[Bu_4N][BzO], was studied with equimolar acid:base concentrations (1:1; 0.10 M in acetonitrile), ensuring that the electrolyte pH was equal to the pK_a of BzOH in acetonitrile, that is, pH = 21.5.[93] These conditions correlate to an equilibrium potential of $E_{CO_2/CO}$ = −1.40 V vs $Fc^{+/0}$ upon application of eq 8. It was observed that under both 0.10 M [BzOH]:[Bu_4N][BzO] acid−base buffer and 0.10 M [Bu_4N]-[BzO] electrolyte conditions, the benzoate anion is strongly coordinating to form the neutral **1-BzO** and **2-BzO** complexes in situ. This was confirmed by variable scan rate analysis in 0.10 M [Bu_4N][BzO] electrolyte under 1 atm of argon where the concerted two-electron reduction peaks for both **1-CH_3CN^+** (−1.63 V) and **2-CH_3CN^+** (−1.60 V) are shifted cathodically to −1.97 and −1.87 V for **1-BzO** and **2-BzO**, respectively (Figures S31 and S32). It is noteworthy that both **1-BzO** and **2-BzO** show quasi-reversible behavior but only corresponding to one-electron equivalent for the reverse anodic peak (Figures S31 and S32). Cyclic voltammetry of **1-BzO** in 0.10 M [BzOH]:[Bu_4N][BzO] (1:1) acetonitrile buffer under 1 atm of CO_2 is presented in Figure 6 with analogous data provided for **2-BzO** in Figure S33. For control conditions, to record i_p under 1 atm of argon, 0.10 M [Bu_4N][BzO] electrolyte was used in acetonitrile. Also, linear sweep voltammetry of **1-CH_3CN^+** and **2-CH_3CN^+** recorded in 0.10 M Bu_4NPF_6 acetonitrile supporting electrolyte under 1 atm of CO_2 upon addition of benzoic acid alone (unknown pH) is provided for comparison in Figure S34.

A consequence of BzO^- coordination is the inherent cathodic shift for both **1-BzO** and **2-BzO**, which adds an overpotential for BzO^- dissociation prior to generation of the two-electron reduced active catalysts **1^-** and **2^-**. Nonetheless, the protonation-first overpotential for the electrocatalytic

DOI: 10.1021/jacs.6b08776
J. Am. Chem. Soc. 2017, 139, 2604−2618

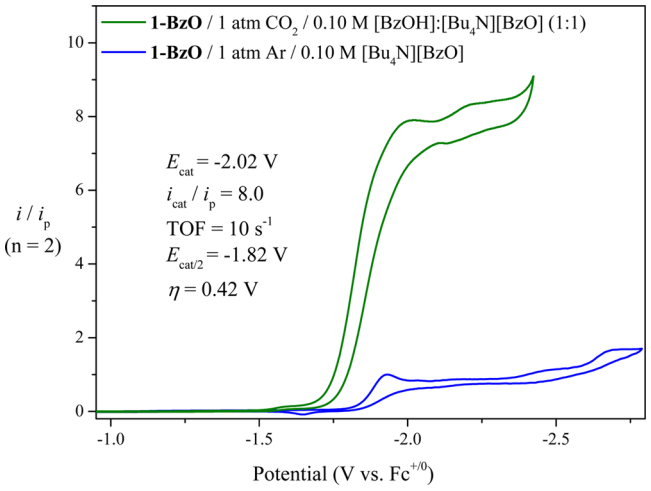

Figure 7. Cyclic voltammetry of **1-BzO** recorded in acetonitrile containing 0.10 M [BzOH]:[Bu_4N][BzO] (1:1) buffer electrolyte under 1 atm of CO_2 (pH = 21.5) and 0.10 M [Bu_4N][BzO] electrolyte under 1 atm of argon. Both scans were recorded at a glassy carbon disc working electrode with a scan rate (υ) of 10 mV s^{-1}.

reduction of CO_2 by **1-BzO** at pH 21.5 in acetonitrile under 1 atm of CO_2 in 0.10 M [BzOH]:[Bu_4N][BzO] electrolyte is calculated as η = 0.42 V (TOF = 10 s^{-1}) in accordance with eq 7, where $E_{CO_2/CO}$ = −1.40 V and $E_{cat/2}$ = −1.82 V (Figure 6). In contrast, **2-BzO** has a slightly higher overpotential at 0.45 V with a lower TOF of 3 s^{-1} (Figure S33). Furthermore, bulk electrolysis experiments confirmed CO as the sole product for both **1-BzO** and **2-BzO** under these conditions.

FTIR Spectroscopy of Reactive Intermediates Relevant to Catalyst Activation and the Catalytic CO_2 Reduction Cycle. We have used pulse radiolysis combined with time-resolved infrared (TRIR) spectroscopy (PR-TRIR) to characterize the intermediate species generated upon one-electron reduction of the two precatalysts under investigation. In a previous PR-TRIR study on the related MnBr(^{t}Bu$_2$-bpy)(CO)$_3$ complex in acetonitrile,[49,94] we made use of formate (HCO_2^-) as an additive to scavenge solvent-derived radicals generated upon pulse radiolysis. It was found that the formate anion replaced the Br^- ligand, resulting in the formation of the Mn−HCO_2 complex before pulse radiolysis. However, upon one-electron reduction, the HCO_2^- ligand was rapidly ejected on the nanosecond time scale to produce the Mn-based radical, $^\bullet$Mn(dtbpy)(CO)$_3$ that was found to dimerize with a rate constant of $2k_{dim}$ = 1.3 × 10^9 M^{-1} s^{-1}.[49] Similarly, in the current experiments, HCO_2^- ligated the precatalysts, resulting in **1-HCO$_2$** and **2-HCO$_2$** as starting materials for the PR-TRIR experiments. Here, we have used a new PR-TRIR detection method, time-resolved step-scan FTIR spectroscopy, the details of which are provided in the Experimental Section.

Figure 8 shows a TRIR spectrum recorded 3 μs after pulse radiolysis of **1-HCO$_2$**. An analogous TRIR spectrum for **2-HCO$_2$** is included in Figure S35. The first species observed in the PR-TRIR experiments is the product of formate ejection following the one-electron reduction of **1-HCO$_2$** and **2-HCO$_2$**. In the case of **1**, this species has two ν(CO) IR bands at 1947 and 1846 cm^{-1} (Figure 7), while for **2**, they occur at 1950 and 1848 cm^{-1} (Figure S35). These are very similar to the two ν(CO) bands of $^\bullet$Mn(^{t}Bu$_2$-bpy)(CO)$_3$ that were previously observed at 1955 and 1853 cm^{-1},[49] leading us to assign the

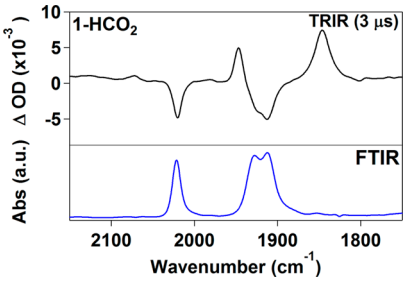

Figure 8. TRIR spectrum of the five-coordinate one-electron reduced species **1**$^\bullet$ (top) recorded 3 μs after pulse radiolysis of an acetonitrile solution of **1-HCO$_2$** containing 0.025 M [Bu_4N][HCO_2] under 1 atm of argon. An FTIR spectrum (bottom) of the solution prior to pulse radiolysis is included for reference.

initial products of one-electron reduction and formate ejection as the five-coordinate Mn-based radicals, $^\bullet$Mn([(MeO)$_2$Ph]$_2$bpy)(CO)$_3$ (**1**$^\bullet$) and $^\bullet$Mn(mes$_2$bpy)(CO)$_3$ (**2**$^\bullet$). Kubiak and co-workers have shown[51,63] that Mn complexes with bulky substituents in the 6,6′ positions of a bpy ligand do not dimerize due to extreme steric hindrance. Our PR-TRIR data agree with this observation, as we saw no evidence for the dimerization of **1**$^\bullet$ or **2**$^\bullet$ into **1**−**1** or **2**−**2** on the micro- to millisecond time scale.

The two-electron reduced five-coordinate active catalyst species **1**$^-$ and **2**$^-$ were investigated by the technique of FTIR spectroelectrochemistry under 1 atm of argon in 0.10 M tetrabutylammonium hexafluorophosphate electrolyte (Table 4). Two ν(CO) IR bands are observed for **2**$^-$ at the lower

Table 4. FTIR Absorption Data in Acetonitrile for All Complexes, Summarizing ν(CO) Stretching Frequencies

complex	ν(CO) (cm^{-1})
1-CH$_3$CN$^+$	2038, 1954, 1941
1$^\bullet$	1947, 1846
1$^-$	1904, 1805
1-CO$^+$	2113, 2038, 2008, 1967
2-CH$_3$CN$^+$	2039, 1948 (br)
2$^\bullet$	1950, 1848
2$^-$	1907, 1806
2-CO$^+$	2106, 2026, 2015 (sh), 1983

stretching frequencies of 1907 and 1806 cm^{-1} (within 2 cm^{-1} of those previously reported[51]) consistent with greater back-bonding onto the CO π* orbitals. Similarly, **1**$^-$ displays two ν(CO) IR bands at 1904 and 1805 cm^{-1}, again consistent with the two-electron reduced five-coordinate assignment as predicted by DFT calculations (Figure S36). By taking advantage of the weakly coordinating OTf^- anion in **1-OTf** and **2-OTf**, we hypothesized that under 1 atm of CO gas in a noncoordinating solvent, such as dichloromethane, the tetracarbonyl species **1-CO$^+$** and **2-CO$^+$** may be generated in situ. Complex **1-CO$^+$** is of specific interest as the immediate product/intermediate following the rate-determining C−OH bond cleavage step in the protonation-first pathway (Scheme 2, intermediate iii). Indeed, the six coordinate tetracarbonyl cation **1-CO$^+$** was formed quantitatively under these conditions. Furthermore, upon removal of the dichloromethane solvent, **1-CO$^+$** remained stable in acetonitrile solvent for comparable FTIR analysis displaying four ν(CO) IR bands at 2113, 2038, 2008, and 1967 cm^{-1} (Figure S36). Although the protonation-

DOI: 10.1021/jacs.6b08776
J. Am. Chem. Soc. 2017, 139, 2604−2618

first pathway is not favored for $\mathbf{2}^-$, it is worthy to note that the analogous **2-CO**$^+$ intermediate could also be characterized in situ displaying four ν(CO) IR bands at 2106, 2026, 2015 (sh), and 1983 cm^{-1} (Figure S37).

Theoretical Investigation of the CO_2 Reduction Mechanism. Density functional theory (DFT) calculations at the M06 level of theory[95] coupled with the SMD continuum solvation method[96] were employed to study the reaction mechanism of CO_2 reduction by **1-CH$_3$CN**$^+$ (see computational methods in the Supporting Information for details). Results for the initial activation and reduction steps of the catalyst are reported in the Supporting Information and are in good agreement with the electrochemical results discussed above (Scheme S1). The computed free energy changes and activation energy for formation of the metallocarboxylic acid **1-CO$_2$H** from the active catalyst $\mathbf{1}^-$ and TFE are provided in Scheme S2. For brevity, only the protonation-first and reduction-first CO_2 reduction pathways are presented in Scheme 3. The initial species in Scheme S2 is the 18-electron

Scheme 3. A Thermodynamic Comparison of Both Protonation-First and Reduction-First Mechanisms of CO_2 Reduction Obtained in Acetonitrile at the M06 Level of Theory,[a] Shown From the 1-COOH Intermediate.

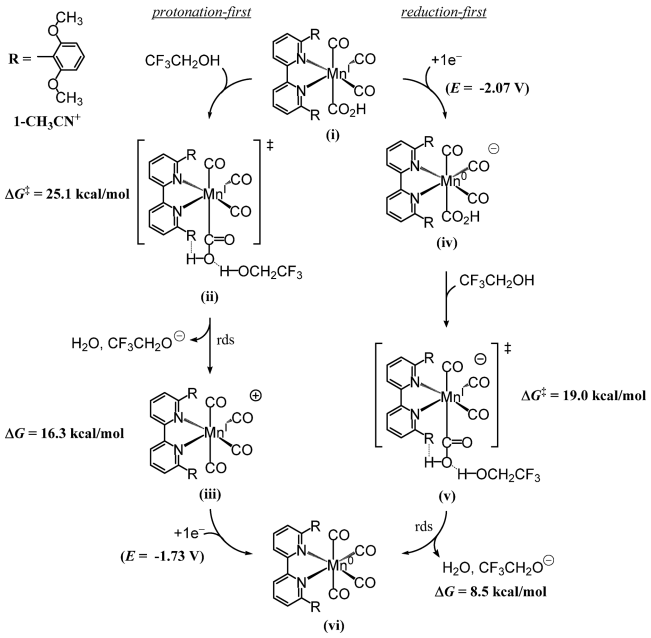

[a]Calculated reduction potentials (E) are reported in units of volts vs $Fc^{+/0}$.

$\mathbf{1}^-$ complex generated via the two-electron-reduction of **1-CH$_3$CN**$^+$. The first step of the proposed mechanism involves binding of CO_2 to $\mathbf{1}^-$, which proceeds with a free energy of activation ($\Delta G^{\ddagger}$) of 10.5 kcal/mol, and the formation of the resulting metallocarboxylate intermediate, **1-CO$_2$**$^-$, is uphill by 8.5 kcal/mol. The protonation of **1-CO$_2$**$^-$ to generate **1-CO$_2$H** (pK_a^{calc} = 26.1) is favorable for PhOH with ΔG = −3.6 kcal/mol and slightly uphill for TFE with ΔG = 6.1 kcal/mol.

Upon formation of the metallocarboxylic acid intermediate **1-CO$_2$H**, the subsequent steps involve C−OH bond breakage to ultimately evolve CO by either the protonation-first or the reduction-first pathways (Scheme 3).[71] The protonation-first pathway starts with cleavage of the C−OH bond in **1-CO$_2$H** with a Brønsted acid as the proton source (e.g., H_2O, MeOH, PhOH, or TFE). The optimized transition state structure with TFE (Figure 9) as the proton source features a $\Delta G^{\ddagger}$ of 25.1 kcal/mol. This protonation step is uphill with ΔG = 16.3 kcal/mol and is followed by a reduction step with an associated computed potential of E = −1.73 V to generate **1-CO**. On the other hand, the initial step of the reduction-first pathway is the reduction of **1-CO$_2$H** to **1-CO$_2$H**$^-$ with a computed potential of E = −2.07 V, followed by protonation and C−OH bond breakage with $\Delta G^{\ddagger}$ = 19.0 kcal/mol with TFE as the proton source. Both the protonation-first and the reduction-first pathways converge at the neutral tetracarbonyl species **1-CO** from where reduction to form **1-CO**$^-$ involves a computed potential of E = −2.54 V. However, reduction of **1-CO** with simultaneous evolution of CO is more favorable, requiring a potential of only E = −1.83 V, and regenerates the active catalyst $\mathbf{1}^-$, completing the catalytic cycle.

For both pathways, cleavage of the C−OH bond is predicted to be rate-determining, so this step was examined more closely with different Brønsted acids as the proton source (Table 5). First, the computed activation free energies ($\Delta G^{\ddagger}$) decrease with increasing acidity (H_2O < MeOH < TFE < PhOH) as expected from the nature of the chemical step. Second, the reduction of **1-CO$_2$H** to **1-CO$_2$H**$^-$ facilitates the C−OH bond breakage as a decrease in $\Delta G^{\ddagger}$'s is observed for all four Brønsted acids examined and becomes especially significant in the case of TFE and PhOH (Table 5). The $\Delta G^{\ddagger}$'s associated with H_2O and MeOH are significantly higher for the protonation-first pathway, which is in line with the experimental observations that H_2O and MeOH are less effective at promoting the protonation-first pathway for **1-CH$_3$CN**$^+$. Furthermore, we also compared the C−OH bond cleavage step for **1-CH$_3$CN**$^+$ versus **2-CH$_3$CN**$^+$. The computed $\Delta G^{\ddagger}$'s are found to be consistently higher for **2-CH$_3$CN**$^+$ as compared to **1-CH$_3$CN**$^+$ for both protonation-first and reduction-first pathways (Table 5), which again is in good agreement with the measured TOFs and the fact that the promotion of the protonation-first pathway is enhanced for **1-CH$_3$CN**$^+$ as compared to **2-CH$_3$CN**$^+$. A comparison of the key geometrical features of the optimized transition states for the protonation-first pathway (Table S2) indicates earlier TS structures for **1-CH$_3$CN**$^+$ as compared to **2-CH$_3$CN**$^+$, as expected from lower $\Delta G^{\ddagger}$'s, and also shows that the ligand framework remains essentially the same (Figure S38). However, there is a significant change in the position and orientation of the Brønsted acids (e.g., TFE) as a result of the C−OH---OMe hydrogen-bonding interaction in **1-CH$_3$CN**$^+$ complexes (C−OH---OMe hydrogen-bond length for the optimized transition states ranges from 1.98 to 2.06 Å). On the basis of these observations, the difference in reactivity of **1-CH$_3$CN**$^+$ as compared to **2-CH$_3$CN**$^+$, especially for the protonation-first pathway, is proposed to stem from a combination of an inductive electronic influence of the pendant methoxy groups of **1-CH$_3$CN**$^+$ and additional stabilization of the C−OH bond cleavage TS via noncovalent hydrogen-bonding interactions between C−OH and the pendant methoxy groups.[97] Finally, we performed benchmark calculations at the DLPNO-CCSD(T) level of theory for the $\Delta G^{\ddagger}$'s associated with the protonation-first pathway for **1-CH$_3$CN**$^+$ and **2-CH$_3$CN**$^+$ to assess the performance of a set of selected density functionals and found that all of the levels of theory employed provide the same qualitative conclusions discussed above (Table S3), and quantitatively the M06-L functional

DOI: 10.1021/jacs.6b08776
J. Am. Chem. Soc. 2017, 139, 2604−2618

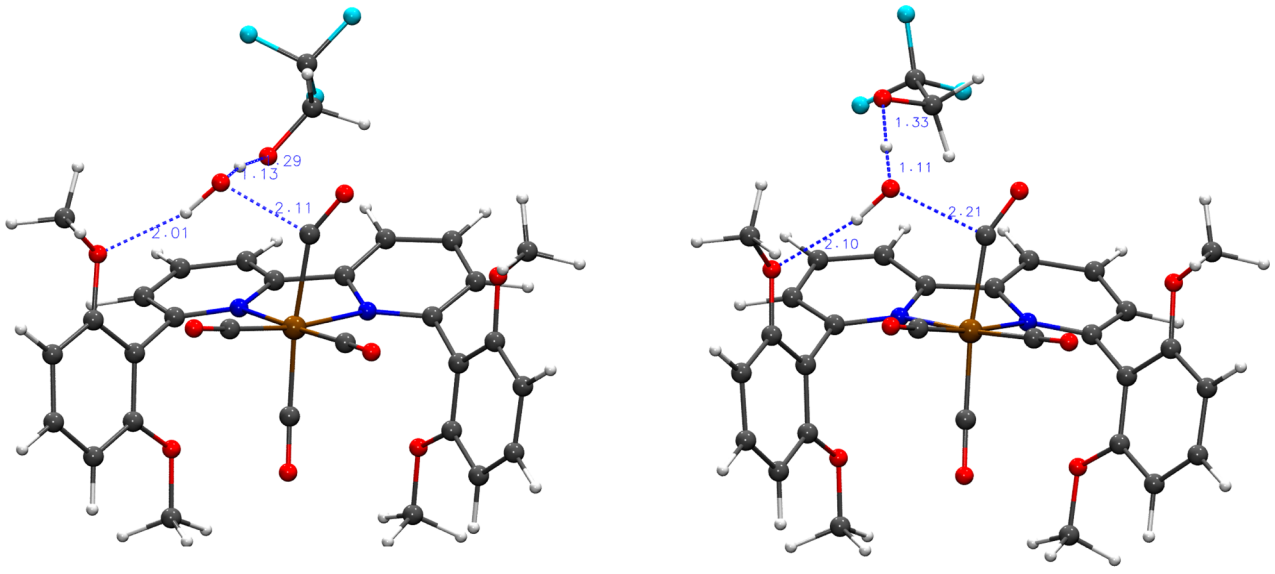

Figure 9. Optimized transition state structures for C−OH bond cleavage for (a) protonation-first and (b) reduction-first pathways. Color code: Mn, ochre; C, gray; N, blue; O, red; H, white.

Table 5. Summary of Computed Free Energies of Activation ($\Delta G^{\ddagger}$) in Units of kcal/mol at the M06 Level of Theory for the C−OH Bond Cleavage Step in Both the Protonation-First and the Reduction-First Pathways

	1-CH_3CN^+				2-CH_3CN^+			
	PhOH	TFE	MeOH	H_2O	PhOH	TFE	MeOH	H_2O
protonation-first	21.0	25.1	29.6	33.2	26.8	30.7	34.1	35.4
reduction-first	16.6	19.0	27.5	32.9	17.7	23.9	28.1	33.1

provides the best agreement with the DLPNO-CCSD(T)[98] level of theory (see computational methods and Supporting Information for further details).

CONCLUSIONS

Electrochemical and computational studies have been utilized to characterize the incipient protonation-first pathway of electrocatalytic reduction of CO_2 to CO for a [*fac*-Mn^I(N^N)-$(CO)_3X]^n$ class of catalyst. Evolution of the protonation-first catalytic pathway, versus the more thermodynamically demanding reduction-first pathway, by **1-CH_3CN^+** exhibits a strong dependence upon the concentration, pK_a, and hence identity of the external weak Brønsted acid proton source in an acetonitrile-based electrolyte, with trifluoroethanol and phenol being the most successful. Efficient access to the sought after protonation-first pathway is thus granted not only by the $[(MeO)_2Ph]_2$bpy ligand in **1-CH_3CN^+** but in combination with the appropriate Brønsted acid proton source. A maximum saving of up to 0.55 V in overpotential is exhibited by the protonation-first pathway for **1-CH_3CN^+** relative to the reduction-first pathway in the presence of 1.37 M PhOH as a Brønsted acid proton source. Access to the protonation-first pathway for **1-CH_3CN^+** has been corroborated by computational studies and is ascribed to a net inductive electronic influence of the pendant methoxy groups of the $(MeO_2Ph)_2$bpy ligand in combination with additional stabilization of the C−OH bond cleavage transition state via noncovalent hydrogen-bonding interactions between C−OH and the pendant methoxy groups. In addition to its enhanced catalytic efficiency at lower overpotential, controlled potential bulk electrolysis studies demonstrate that **1-CH_3CN^+** also exhibits excellent product selectivity for CO evolution in the presence of nonaqueous Brønsted acid proton sources, MeOH, TFE, and PhOH. To probe catalyst activation, the technique of time-resolved infrared spectroscopy combined with pulse-radiolysis (PR-TRIR) was used to cleanly observe the ν(CO) vibrational frequencies of the neutral, one-electron reduced, 5-coordinate precatalyst species **1**$^\bullet$ (1947, 1846 cm^{-1}) and **2**$^\bullet$ (1950, 1848 cm^{-1}). FTIR spectra of the anionic, two-electron reduced, 5-coordinate active catalyst species **1**$^-$ (1904, 1805 cm^{-1}) and **2**$^-$ (1907, 1806 cm^{-1}) were obtained by spectroelectrochemistry, and ν(CO) vibrational frequencies of the key cationic, six-coordinate tetracarbonyl catalytic intermediates **1-CO**$^+$ (2113, 2038, 2008, 1967 cm^{-1}) and **2-CO**$^+$ (2106, 2026, 2015 (sh), 1983 cm^{-1}) have also been reported. Finally, on the basis of the standard potential for the reduction of CO_2 to CO in dry acetonitrile at pH 0, it has been possible to report the true electrocatalytic overpotential for both active catalysts **1**$^-$ and **2**$^-$ in acetonitrile in the presence of an acid−base buffer at a pH of 21.5.

EXPERIMENTAL SECTION

Materials and Methods. The following chemicals were purchased from Sigma-Aldrich: bromopentacarbonylmanganese(I) (98%), silver trifluoromethanesulfonate (>99%), 2,4,6-trimethylphenylboronic acid, 2,6-dimethoxyphenylboronic acid, tetrabutylammonium hexafluorophosphate (>99%), tetrabutylammonium benzoate (>99%), benzoic acid (>99%), potassium carbonate (>99%), tetrabutylammonium trifluoromethanesulfonate (>99%), trifluoromethanesulfonic acid (>99%), methanol (spectrophotometric grade), D_2O (99.9% D), 2,2,2-trifluoroethanol (>99%), phenol (>99.9%), and acetonitrile

DOI: 10.1021/jacs.6b08776
J. Am. Chem. Soc. 2017, 139, 2604−2618

(electronic grade, 99.999%). Tetrakis(triphenylphosphine)-palladium(0) (99%) and 6,6′-dibromo-2,2′-bipyridine (>95%) were purchased from Strem and TCI America, respectively. Tetrabutylammonium hexafluorophosphate was recrystallized thrice from ethanol and dried under vacuum prior to electrolyte preparation. Gas cylinders were ordered from Airgas containing premixed ratios of Ar:CO_2 (100:0, 80:20, 60:40, 50:50, 40:60, 20:80, 0:100). FTIR spectra were recorded on a Thermo Nicolet 670 FTIR spectrophotometer in spectrophotometric grade acetonitrile. NMR spectra were recorded on an Agilent spectrometer operated at 399.80 MHz for ^{1}H and 100.54 MHz for ^{13}C nuclei. Deuterated solvents d_6-DMSO and CD_3CN were used as received from Sigma-Aldrich, and their residual ^{1}H and ^{13}C solvent signals[99] were used as internal references for reporting the chemical shift (δ). ^{1}H NMR spectra of **2-CD_3CN^+** and FTIR of **2-CH_3CN^+** were consistent with literature reports.[51] LC−MS of $[(MeO)_2Ph]_2bpy$ was performed on an Agilent 2100 system using atmospheric pressure chemical ionization (APCI) mode. Mobile phases consisted of methanol and water both containing 0.05% trifluoroacetic acid. A linear gradient was used to increase from 25:75 v/v methanol/water to 100% methanol over 7.0 min at a flow rate of 0.7 mL/min with a C18 (5.0 μm, 6.0 × 50 mm) column. UV detection of the eluent was conducted at 210, 254, and 365 nm. Voltammetry and bulk electrolysis were carried out on a CH Instruments 620E potentiostat. A custom three-electrode cell was used for both voltammetry and bulk electrolysis experiments, allowing airtight introduction of working, counter, and reference electrodes as well as septa for gas purging. For cyclic voltammetry, glassy carbon (3 mm diameter) and Pt wire were used as working and counter electrodes, respectively, with 0.1 M Bu_4NPF_6 in spectrophotometric grade acetonitrile as the supporting electrolyte. A nonaqueous reference electrode was used to minimize ohmic potential drop at the solvent interface. This consisted of a Ag wire in 0.10 M Bu_4NPF_6 acetonitrile supporting electrolyte isolated by a Vycor frit and was calibrated in situ using the ferrocenium/ferrocene redox couple as a pseudo reference. Redox potentials (E) were determined from cyclic voltammetry as (E_{pa} + E_{pc})/2, where E_{pa} and E_{pc} are the anodic and cathodic peak potentials, respectively. Where E could not be calculated due to irreversible behavior, E_{pc} and E_{pa} are reported accordingly. For electrocatalysis studies, all observed currents were corrected for a dilution factor upon addition of various volumes of each Brønsted acid. For controlled potential bulk electrolysis experiments, a vitreous carbon (Structure Probe, Inc.) working electrode soldered to a copper wire was used. A Pt gauze counter electrode was used, isolated from the main compartment by a fine porosity Vycor tube+frit to minimize mass transfer resistance. Gas chromatography data were recorded on a custom Shimadzu GC-2014 instrument where a Ni "methanizer" catalyst was used to convert CO to CH_4 prior to quantification of CH_4 by the thermal conductivity detector (TCD detectors have poor sensitivity for CO and high sensitivity for CH_4). H_2 was simultaneously monitored by a flame ionization detector during the same injection. The GC was precalibrated for CO and H_2 quantification by mimicking bulk electrolysis conditions (i.e., 5 mL of supporting electrolyte in the same cell, with electrodes, under 1 atm of CO_2). Standard curves for H_2 and CO were generated using this cell where known volumes of the analyte gas (H_2 or CO) were injected, and the solution was stirred for 30 min to allow equilibration of the analyte between the electrolyte and headspace prior to GC injection.

Synthesis. *6,6′-Bis(2,6-dimethoxyphenyl)-2,2′-bipyridine $[(MeO)_2Ph]_2bpy$.* One hundred milligrams of 6,6′-dibromo-2,2′-bipyridine (0.312 mmol) and 144 mg of (2,6-dimethoxyphenyl)-boronic acid (0.936 mmol, 3 equiv) were added to a 5 mL microwave tube. One milliliter of 2 M aqueous Na_2CO_3 and 1 mL of toluene were added to the reaction tube, and the mixture was purged with argon for 5 min. Eighteen milligrams of tetrakis(triphenylphosphine)-palladium(0) (0.0156 mmol, 0.05 equiv) was added to the reaction tube followed by 1 mL of ethanol with further argon purging. The reaction tube was sealed and irradiated with microwaves at 120 °C for 1 h. Upon completion, the reaction mixture was extracted with dichloromethane. The combined organic layer was washed with brine solution and dried with $MgSO_4$. The volume of dichloromethane was reduced under vacuum to approximately 0.5 mL, 20 mL of methanol was added, and the mixture was cooled in the freezer for 1 h. A white solid precipitated and was collected by vacuum filtration. The product was washed with cold methanol and dried under vacuum overnight, realizing 120 mg (90% yield) of pure product. LC−MS predicted (M + 1) = 429.2 m/z; observed (M + 1) = 429.2 m/z. ^{1}H NMR [$(CD_3)_2SO$]: δ = 8.18 (d, 2H, 3,3′-bpy-H, J = 8 Hz), 7.87 (t, 2H, 5,5′-bpy-H, J = 8 Hz), 7.39 (t, 2H, 4,4′-bpy-H, J = 8 Hz), 7.27 (d, 2 para H, phenyl-H, J = 8 Hz), 6.79 (d, 4H, 4 meta H phenyl-H, J = 8 Hz), 3.68 (s, 12H, 4 ortho OCH_3). ^{13}C NMR [$(CD_3)_2SO$]: δ = 158.17, 155.66, 154.37, 137.30, 130.24, 129.38, 126.59, 119.46, 104.99, 56.30 ppm.

fac-Mn^I([(MeO)$_2$Ph]$_2$bpy)(CO)$_3$(OTf) ***1-OTf.*** Following a reported procedure for the synthesis of *fac*-$Mn(CO)_5(OTf)$,[72] bromopentacarbonylmanganese(I) (67.6 mg, 0.241 mmol) was added to 25 mL of dichloromethane in a 50 mL round-bottom flask under 1 atm of argon. Silver triflate (62.6 mg, 0.241 mmol) was added, and the reaction mixture was allowed to stir in the dark. After 3 h, the reaction mixture was filtered through a Celite plug by vacuum filtration to remove the resulting AgBr precipitate. The filtrate was dried by rotary evaporation, quantitatively yielding *fac*-$Mn(CO)_5(OTf)$ as a yellow solid confirmed by FTIR spectroscopy.[72] This product was dissolved in 25 mL of diethyl ether in a 50 mL round-bottom flask, and the ligand 6,6′-bis(2,6-dimethoxyphenyl)-2,2′-bipyridine (76 mg, 0.181 mmol) was added under 1 atm of argon. The reaction mixture was refluxed in the dark for 3 h and cooled to room temperature. The yellow precipitate was collected by vacuum filtration, washed with cold diethyl ether, and dried under vacuum overnight in a sealed round-bottom flask, yielding 97 mg (75%). ^{1}H NMR of **1-CD_3CN^+** (CD_3CN): δ = 8.43, 8.41 (dd, 2H, 3,3′-bpy-H, J = 1, J_d = 2), δ = 8.19 (t, 2H, 5,5′-bpy-H, J = 2), δ = 7.50 (m, 4H, 4,4′-bpy-H and para H phenyl), δ = 6.79 (dd, 4H, meta H phenyl, J_d = 2), δ = 3.76 (s, 6H, 2OCH_3), δ = 3.68 (s, 6H, 2OCH_3). FTIR of **1-CH_3CN^+** in CH_3CN ν(CO): 2038, 1954, 1941 cm^{-1}. Anal. Calcd for **1** $C_{30}H_{24}F_3MnN_2O_{10}S$: C, 50.29; H, 3.38; N, 3.91. Found: C, 50.11; H, 3.32; N, 3.84.

Pulse Radiolysis Step-Scan FTIR Experiments. The pulse radiolysis experiments were conducted at the 2 MeV Van de Graaff (VdG) electron accelerator located in the Chemistry Division at Brookhaven National Laboratory. A commercial step-scan FTIR spectrometer (Bruker, IFS 66/S) equipped with an external fast rise time HgCdTe IR detector was placed on an air-stabilized optical bench close to the VdG's electron beamline exit window, with the electron beam passing directly through a homemade, airtight IR flow cell (0.7 mm path length) equipped with 0.5 mm thick CaF_2 windows. A 25 mL CH_3CN solution containing 1.5 mM of the Mn complex and 0.025 M tetrabutylammonium formate (synthesized according to a reported procedure[49]) was prepared inside a glovebox and placed into a sealed reservoir vessel. The vessel was then inserted into a gastight recirculating flow system containing a magnetically coupled gear pump (Micropump). The tubing was evacuated and refilled with argon several times before saturating the solution with 2 atm of argon and flowing. The VdG can produce electron pulses of increasing dose by increasing the electron pulsewidth up to a maximum of 4 μs. In these experiments, we used 1 μs electron pulses at a repetition rate of 5 Hz. Because our experiments were not quantitative, we did not measure the absorbed dose. The time-resolved step-scan FTIR measurements were performed in a manner similar to those previously reported[100] for laser flash photolysis, except in this case a digital delay generator (Stanford Research Systems, DG535) was used to trigger the electron pulses in synchronization with the data collection. A 1 MHz preamplifier (Stanford Research Systems, SR560) was used to amplify the detector signal prior to digitization. In a typical experiment, data were collected at 6 cm^{-1} spectral resolution with an optical band-pass filter that resulted in 252 interferogram mirror positions. Either 4 or 8 averages were acquired at each mirror position, leading to a total of either 1008 or 2016 electron pulses impinging on the flowing sample. FTIR spectra recorded after the experiment showed very little overall sample decomposition (<5%).

DOI: 10.1021/jacs.6b08776
J. Am. Chem. Soc. 2017, 139, 2604−2618

■ ASSOCIATED CONTENT

Supporting Information

The Supporting Information is available free of charge on the ACS Publications website at DOI: 10.1021/jacs.6b08776.

NMR spectra, additional voltammetry, FTIR, bulk electrolysis, computational, and Cartesian coordinate data (PDF)

■ AUTHOR INFORMATION

Corresponding Authors

*dcgrills@bnl.gov
*mzertem@bnl.gov
*jonathan.rochford@umb.edu

ORCID

David C. Grills: 0000-0001-8349-9158
Jonathan Rochford: 0000-0003-2397-9162

Notes

The authors declare no competing financial interest.

■ ACKNOWLEDGMENTS

J.R. thanks the National Science Foundation for support under grant number CHE-1301132. The work at BNL (D.C.G. and M.Z.E.) and use of the Van de Graaff facility of the BNL Accelerator Center for Energy Research were supported by the U.S. Department of Energy (DOE), Office of Basic Energy Sciences, Division of Chemical Sciences, Geosciences & Biosciences, under contract no. DE-SC0012704. K.T.N. is grateful to the DOE for an Office of Science Graduate Student Research (SCGSR) award. This research used resources of the Center for Functional Nanomaterials (CFN) for the fabrication of optics for PR-TRIR experiments. The CFN is a U.S. DOE Office of Science Facility, at Brookhaven National Laboratory operating under Contract No. DE-SC0012704.

■ REFERENCES

(1) U.S. Department of Commerce, National Oceanic and Atmospheric Administration, Earth System Research Laboratory, Global Monitoring Division; http://www.esrl.noaa.gov/gmd/ccgg/trends/index.html (accessed July 19th 2016).
(2) Cocks, H. F. *Energy Demand and Climate Change*; Wiley-VCH: New York, 2009.
(3) Zhang, Q. H.; Kang, J. C.; Wang, Y. *ChemCatChem* **2010**, *2*, 1030−1058.
(4) Matsubara, Y.; Grills, D. C.; Kuwahara, Y. *ACS Catal.* **2015**, *5*, 6440−6452.
(5) Arakawa, H.; Areasta, M.; Armor, J. N.; Barteau, M. A.; Beckman, E. J.; Bell, A. T.; Bertcaw, J. E.; Creutz, C.; Dinjus, E.; Dixon, D. A.; Domen, K.; DuBois, D. L.; Eckert, J.; Fujita, E.; Gibson, D. H.; Goddart, W. A.; Goodman, D. W.; Keller, J.; Kubas, G. J.; Kung, H. H.; Lyons, J. E.; Manzer, L. E.; Marks, T. J.; Morokuma, K.; Nicholas, K. M.; Periana, R.; Que, L.; Rostrup-Nielsen, J. R.; Sachtler, W. M. H.; Schmidt, L. D.; Sen, A.; Somorjai, J. A.; Stair, P. C.; Stults, B. R.; Tumas, W. *Chem. Rev.* **2001**, *101*, 953−996.
(6) Costentin, C.; Drouet, S.; Robert, M.; Saveant, J. M. *Science* **2012**, *338*, 90−94.
(7) Pegis, M. L.; Roberts, J. A. S.; Wasylenko, D. J.; Mader, E. A.; Appel, A. M.; Mayer, J. M. *Inorg. Chem.* **2015**, *54*, 11883−11888.
(8) Qiao, J. L.; Liu, Y. Y.; Hong, F.; Zhang, J. J. *Chem. Soc. Rev.* **2014**, *43*, 631−675.
(9) Keene, F. R.; Sullivan, B. P. In *Electrochemical and Electrocatalytic Reactions of Carbon Dioxide*; Sullivan, B. P., Krist, K., Guard, H. E., Eds.; Elsevier: New York, 1993; pp 1−18.
(10) Leitner, W. *Coord. Chem. Rev.* **1996**, *153*, 257−284.
(11) Fischer, B. J.; Eisenberg, R. G. *J. Am. Chem. Soc.* **1980**, *102*, 7361−7363.
(12) Beley, M.; Collin, J. P.; Ruppert, R.; Sauvage, J. P. *J. Am. Chem. Soc.* **1986**, *108*, 7461−7467.
(13) Schneider, J.; Jia, H.; Kobiro, K.; Cabelli, D. E.; Muckerman, J. T.; Fujita, E. *Energy Environ. Sci.* **2012**, *5*, 9502−9510.
(14) Schneider, J.; Jia, H.; Muckerman, J. T.; Fujita, E. *Chem. Soc. Rev.* **2012**, *41*, 2036−2051.
(15) Lacy, D. C.; McCrory, C. C. L.; Peters, J. C. *Inorg. Chem.* **2014**, *53*, 4980−4988.
(16) Chen, L.; Guo, Z.; Wei, X.-G.; Gallenkamp, C.; Bonin, J.; Anxolabehere-Mallart, E.; Lau, K.-C.; Lau, T.-C.; Robert, M. *J. Am. Chem. Soc.* **2015**, *137*, 10918−10921.
(17) Manbeck, G. F.; Fujita, E. *J. Porphyrins Phthalocyanines* **2015**, *19*, 45−64.
(18) Costentin, C.; Robert, M.; Saveant, J. M. *Acc. Chem. Res.* **2015**, *48*, 2996−3006.
(19) Lin, S.; Diercks, C. S.; Zhang, Y. B.; Kornienko, N.; Nichols, E. M.; Zhao, Y. B.; Paris, A. R.; Kim, D.; Yang, P.; Yaghi, O. M.; Chang, C. J. *Science* **2015**, *349*, 1208−1213.
(20) Chan, S. L.-F.; Lam, T. L.; Yang, C.; Yan, S.-C.; Cheng, N. M. *Chem. Commun.* **2015**, *51*, 7799−7801.
(21) Elgrishi, N.; Chambers, M. B.; Fontecave, M. *Chem. Sci.* **2015**, *6*, 2522−2531.
(22) Chapovetsky, A.; Do, T. H.; Haiges, R.; Takase, M. K.; Marinescu, S. C. *J. Am. Chem. Soc.* **2016**, *138*, 5765−5768.
(23) Hawecker, J.; Lehn, J. M.; Ziessel, R. *J. Chem. Soc., Chem. Commun.* **1984**, 328−330.
(24) Keith, J. A.; Grice, K. A.; Kubiak, C. P.; Carter, E. A. *J. Am. Chem. Soc.* **2013**, *135*, 15823−15829.
(25) Manbeck, G. F.; Muckerman, J. T.; Szalda, D. J.; Himeda, Y.; Fujita, E. *J. Phys. Chem. B* **2015**, *119*, 7457−7466.
(26) Franco, F.; Cometto, C.; Garino, C.; Minero, C.; Sordello, F.; Nervi, C.; Gobetto, R. *Eur. J. Inorg. Chem.* **2015**, *2015*, 296−304.
(27) Ishida, H.; Tanaka, K.; Tanaka, T. *Organometallics* **1987**, *6*, 181−186.
(28) Nagao, H.; Mizukawa, T.; Tanaka, K. *Inorg. Chem.* **1994**, *33*, 3415−3420.
(29) Tanaka, K.; Ooyama, D. *Coord. Chem. Rev.* **2002**, *226*, 211−218.
(30) Chen, Z.; Chen, C.; Weinberg, D. R.; Kang, P.; Concepcion, J. J.; Harrison, D. P.; Brookhart, M. S.; Meyer, T. J. *Chem. Commun.* **2011**, *47*, 12607−12609.
(31) Johnson, B. A.; Maji, S.; Agarwala, H.; White, T. A.; Mijangos, E.; Ott, S. *Angew. Chem., Int. Ed.* **2016**, *55*.
(32) Bruce, M. R. M.; Megehee, E.; Sullivan, B. P.; Thorp, H. H.; O'Toole, T. R.; Downard, A.; Pugh, J. R.; Meyer, T. J. *Inorg. Chem.* **1992**, *31*, 4864−4873.
(33) Bolinger, C. M.; Story, N.; Sullivan, B. P.; Meyer, T. J. *Inorg. Chem.* **1988**, *27*, 4582−4587.
(34) Sypaseuth, F. D.; Matlachowski, C.; Weber, M.; Schwalbe, M.; Tzschucke, C. C. *Chem. - Eur. J.* **2015**, *21*, 6564−6571.
(35) Haines, R. J.; Wittrig, R. E.; Kubiak, C. P. *Inorg. Chem.* **1994**, *33*, 4723−4728.
(36) Delaet, D. L.; Delrosario, R.; Fanwick, P. E.; Kubiak, C. P. *J. Am. Chem. Soc.* **1987**, *109*, 754−758.
(37) Slater, S.; Wagenknecht, J. H. *J. Am. Chem. Soc.* **1984**, *106*, 5367−5368.
(38) Raebiger, J. W.; Turner, J. W.; Noll, B. C.; Curtis, C. J.; Miedaner, A.; Cox, B.; DuBois, D. L. *Organometallics* **2006**, *25*, 3345−3351.
(39) Fujita, E.; Brunschwig, B. S. In *Catalysis, Heterogeneous Systems, Gas Phase Systems, Electron Transfer in Chemistry*; Balzani, V., Ed.; Wiley-VCH: New York, 2001; Vol.4, pp 88−126.
(40) Morris, A. J.; Meyer, G. J.; Fujita, E. *Acc. Chem. Res.* **2009**, *42*, 1983−1994.
(41) Benson, E. E.; Kubiak, C. P.; Sathrum, A. J.; Smieja, J. M. *Chem. Soc. Rev.* **2009**, *38*, 89−99.
(42) Doherty, M. D.; Grills, D. C.; Muckerman, J. T.; Polyansky, D. E.; Fujita, E. *Coord. Chem. Rev.* **2010**, *254*, 2472−2482.

DOI: 10.1021/jacs.6b08776
J. Am. Chem. Soc. 2017, 139, 2604−2618

(43) Takeda, H.; Ishitani, O. *Coord. Chem. Rev.* **2010**, *254*, 346−354.
(44) Mikkelsen, M.; Jorgensen, M.; Krebs, F. C. *Energy Environ. Sci.* **2010**, *3*, 43−81.
(45) Hawecker, J.; Lehn, J. M.; Ziessel, R. *Helv. Chim. Acta* **1986**, *69*, 1990−2012.
(46) Grills, D. C.; Fujita, E. *J. Phys. Chem. Lett.* **2010**, *1*, 2709−2718.
(47) Bourrez, M.; Molton, F.; Chardon-Noblat, S.; Deronzier, A. *Angew. Chem., Int. Ed.* **2011**, *50*, 9903−9906.
(48) Smieja, J. M.; Sampson, M. D.; Grice, K. A.; Benson, E. E.; Froehlich, J. D.; Kubiak, C. P. *Inorg. Chem.* **2013**, *52*, 2484−2491.
(49) Grills, D. C.; Farrington, J. A.; Layne, B. H.; Lymar, S. V.; Mello, B. A.; Preses, J. M.; Wishart, J. F. *J. Am. Chem. Soc.* **2014**, *136*, 5563−5566.
(50) Franco, F.; Cometto, C.; Vallana, F. F.; Sordello, F.; Priola, E.; Minero, C.; Nervi, C.; Gobetto, R. *Chem. Commun.* **2014**, *50*, 14670−14673.
(51) Sampson, M. D.; Nguyen, A. D.; Grice, K. A.; Moore, C. E.; Rheingold, A. L.; Kubiak, C. P. *J. Am. Chem. Soc.* **2014**, *136*, 5460−5471.
(52) Riplinger, C.; Sampson, M. D.; Ritzmann, A. M.; Kubiak, C. P.; Carter, E. A. *J. Am. Chem. Soc.* **2014**, *136*, 16285−16298.
(53) Takeda, H.; Koizumi, H.; Okamoto, K.; Ishitani, O. *Chem. Commun.* **2014**, *50*, 1491−1493.
(54) Orio, M. B. M.; Molton, F.; Vezin, H.; Duboc, C.; Deronzier, A.; Chardon-Noblat, S. *Angew. Chem., Int. Ed.* **2014**, *53*, 240−243.
(55) Agarwal, J.; Shaw, T. W.; Stanton, C. J.; Majetich, G. F.; Bocarsly, A. B.; Schaefer, H. F. *Angew. Chem., Int. Ed.* **2014**, *53*, 5152−5155.
(56) Zeng, Q.; Tory, J.; Hartl, F. *Organometallics* **2014**, *33*, 5002−5008.
(57) Walsh, J. J.; Smith, C. L.; Neri, G.; Whitehead, G. F. S.; Robertson, C. M.; Cowan, A. J. *Faraday Discuss.* **2015**, *183*, 147−160.
(58) Grice, K. A.; Kubiak, C. P.; Aresta, M.; Eldik, R. V. *Adv. Inorg. Chem.* **2014**, *66*, 163−188.
(59) Machan, C. W.; Stanton, C. J.; Vandezande, J. E.; Majetich, G. F.; Schaefer, H. F.; Kubiak, C. P.; Agarwal, J. *Inorg. Chem.* **2015**, *54*, 8849−8856.
(60) Riplinger, C.; Carter, E. A. *ACS Catal.* **2015**, *5*, 900−908.
(61) Lam, Y. C.; Nielsen, R. J.; Gray, H. B.; Goddard, W. A. *ACS Catal.* **2015**, *5*, 2521−2528.
(62) Agarwal, J.; Shaw, T. W.; Schaefer, H. F.; Bocarsly, A. B. *Inorg. Chem.* **2015**, *54*, 5285−5294.
(63) Sampson, M. D.; Kubiak, C. P. *J. Am. Chem. Soc.* **2016**, *138*, 1386−1393.
(64) Rao, G. K.; Pell, W.; Korobkov, I.; Richeson, D. *Chem. Commun.* **2016**, *52*, 8010−8013.
(65) Rawat, K. S.; Mahata, A.; Choudhuri, I.; Pathak, B. *J. Phys. Chem. C* **2016**, *120*, 8821−8831.
(66) Hammouche, M.; Lexa, D.; Momenteau, M.; Saveant, J. M. *J. Am. Chem. Soc.* **1991**, *113*, 8455−8466.
(67) Bhugun, I.; Lexa, D.; Saveant, J. M. *J. Phys. Chem.* **1996**, *100*, 19981−19985.
(68) Fujita, E.; Chou, M.; Tanaka, K. *Appl. Organomet. Chem.* **2000**, *14*, 844−846.
(69) Bhugun, I.; Lexa, D.; Saveant, J. M. *J. Am. Chem. Soc.* **1996**, *118*, 1769−1776.
(70) Costentin, C.; Passard, G.; Robert, M.; Saveant, J. M. *Proc. Natl. Acad. Sci. U. S. A.* **2014**, *111*, 14990−14994.
(71) Riplinger, C.; Carter, E. A. *ACS Catal.* **2015**, *5*, 900−908.
(72) Scheiring, T.; Kaim, W.; Fiedler, J. *J. Organomet. Chem.* **2000**, *598*, 136−141.
(73) Veghini, D.; Berke, H. *Inorg. Chem.* **1996**, *35*, 4770−4778.
(74) Dattelbaum, D. M.; Omberg, K. M.; Schoonover, J. R.; Martin, R. L.; Meyer, T. J. *Inorg. Chem.* **2002**, *41*, 6071−6079.
(75) Rountree, E. S.; McCarthy, B. D.; Eisenhart, T. T.; Dempsey, J. L. *Inorg. Chem.* **2014**, *53*, 9983−10002.
(76) Costentin, C.; Passard, G.; Saveant, J. M. *J. Am. Chem. Soc.* **2015**, *137*, 5461−5467.
(77) Costentin, C.; Robert, M.; Saveant, J. M. *Chem. Soc. Rev.* **2013**, *42*, 2423−2436.
(78) Costentin, C.; Drouet, S.; Robert, M.; Saveant, J. M. *J. Am. Chem. Soc.* **2012**, *134*, 11235−11242.
(79) Saveant, J. M. *Chem. Rev.* **2008**, *108*, 2348−2378.
(80) Savéant, J. M.; Su, K. B. *J. Electroanal. Chem. Interfacial Electrochem.* **1984**, *171*, 341−349.
(81) Martin, D. J.; McCarthy, B. D.; Rountree, E. S.; Dempsey, J. L. *Dalton Trans.* **2016**, *45*, 9970−9976.
(82) Grills, D. C.; Matsubara, Y.; Kuwahara, Y.; Golisz, S. R.; Kurtz, D. A.; Mello, B. A. *J. Phys. Chem. Lett.* **2014**, *5*, 2033−2038.
(83) Andrieux, C. P.; Blocman, C.; Dumas-Bouchiat, J. M.; M'Halla, F.; Savéant, J. M. *J. Electroanal. Chem. Interfacial Electrochem.* **1980**, *113*, 19−40.
(84) Costentin, C.; Savéant, J.-M. *ChemElectroChem* **2014**, *1*, 1226−1236.
(85) Olmstead, W. N.; Margolin, Z.; Bordwell, F. G. *J. Org. Chem.* **1980**, *45*, 3295−3299.
(86) Bordwell, F. G. *Acc. Chem. Res.* **1988**, *21*, 456−463.
(87) Bordwell, F. G.; McCallum, R. J.; Olmstead, W. N. *J. Org. Chem.* **1984**, *49*, 1424−1427.
(88) Raamat, E.; Kaupmees, K.; Ovsjannikov, G.; Trummal, A.; Kütt, A.; Saame, J.; Koppel, I.; Kaljurand, I.; Lipping, L.; Rodima, T.; Pihl, V.; Koppel, I. A.; Leito, I. *J. Phys. Org. Chem.* **2013**, *26*, 162−170.
(89) Liyanage, N. P.; Dulaney, H. A.; Huckaba, A. J.; Jurss, J. W.; Delcamp, J. H. *Inorg. Chem.* **2016**, *55*, 6085−6094.
(90) Narayanan, R.; McKinnon, M.; Reed, B. R.; Ngo, K. T.; Groysman, S.; Rochford, J. *Dalton Trans.* **2016**, *45*, 15285−15289.
(91) Walsh, J. J.; Neri, G.; Smith, C. L.; Cowan, A. J. *Chem. Commun.* **2014**, *50*, 12698−12701.
(92) Appel, A. M.; Helm, M. L. *ACS Catal.* **2014**, *4*, 630−633.
(93) Kütt, A.; Leito, I.; Kaljurand, I.; Sooväli, L.; Vlasov, V. M.; Yagupolskii, L. M.; Koppel, I. A. *J. Org. Chem.* **2006**, *71*, 2829−2838.
(94) Grills, D. C.; Farrington, J. A.; Layne, B. H.; Preses, J. M.; Bernstein, H. J.; Wishart, J. F. *Rev. Sci. Instrum.* **2015**, *86*.
(95) Zhao, Y.; Truhlar, D. G. *Theor. Chem. Acc.* **2008**, *120*, 215−241.
(96) Marenich, A. V.; Cramer, C. J.; Truhlar, D. G. *J. Phys. Chem. B* **2009**, *113*, 6378−6396.
(97) Grabowski, S. J.; Sokalski, W. A.; Dyguda, E.; Leszczyński, J. *J. Phys. Chem. B* **2006**, *110*, 6444−6446.
(98) Riplinger, C.; Sandhoefer, B.; Hansen, A.; Neese, F. *J. Chem. Phys.* **2013**, *139*.
(99) Fulmer, G. R.; Miller, A. J. M.; Sherden, N. H.; Gottlieb, H. E.; Nudelman, A.; Stoltz, B. M.; Bercaw, J. E.; Goldberg, K. I. *Organometallics* **2010**, *29*, 2176−2179.
(100) Grills, D. C.; van Eldik, R.; Muckerman, J. T.; Fujita, E. *J. Am. Chem. Soc.* **2006**, *128*, 15728−15741.

DOI: 10.1021/jacs.6b08776
J. Am. Chem. Soc. 2017, 139, 2604−2618